Geology of the Mutis Complex, Miomaffo, West Timor

R. Berry[a,*], K. Goemann[b], L. Danyushevsky[a] & E. Lounejeva[a]

[a]Centre for Ore Deposit and Earth Sciences, University of Tasmania, Tasmania, Australia; [b]Central Science Laboratory, University of Tasmania, Tasmania, Australia

Mail: Centre for Ore Deposit and Earth Sciences, University of Tasmania, Private Bag 79, Hobart, Tasmania 7001, Australia

Ron Berry 0000-0002-5547-3396

Karsten Goemann 0000-0002-8136-3617

Leonid Danyushevsky 0003-4050-6850

Elena Lounejeva 0000-0002-2462-8623

* Corresponding Author: Ron Berry email Ron.Berry@utas.edu.au

Karsten.Goemann@utas.edu.au

leonid6@bigpond.com

Elena.Lounejeva@utas.edu.au

Supplemental data files

Supplemental_Text.pdf
Supplemental_Tables.xlsx
Containing:
    Supplemental data 1. pXRF analysis of rocks from the Miomaffo massif.
        SD1/Table 1. Whole rock composition estimates from portable XRF.
    Supplemental data 2. Whole rock geochemical analyses of basalts and dykes, Miomaffo.
        SD2/Table 1. Whole rock geochemistry.
    Supplemental data 3. Unpublished K/Ar and Ar/Ar data of the Mutis Complex, Miomaffo.
        SD3/Table 1. K/Ar hornblende age for amphibolites from Mutis Complex rocks at Miomaffo.
        SD3/Table 2. Ar/Ar hornblende age data for Western Sector amphibolites in the Mutis Complex at Miomaffo.
        SD3/Table 3. Ar/Ar hornblende age data for amphibolite block in Eastern Sector melange, Mutis Complex, Miomaffo.
    Supplemental data 4. U/Pb Zircon age for three samples from the Mutis Complex, Miomaffo.
        SD4/Table 1. LA-ICP-MS analyses of zircon.
    Supplemental data 5. Metamorphic history of the Mutis Complex, Miomaffo.
        SD5/Table 1. Composition of common minerals. Stoichiometry calculated using AX (Powell & Holland, 2008).
        SD5/Table 2. SEM point counted mineralogy from six metamorphic rocks.
    Supplemental data 6. U/Pb Apatite age for a garnet gneiss of the Mutis Complex, Miomaffo.
        SD6/Table 1. Sample 63725 LA ICP-MS analysis of apatite.

Supplemental data 1. pXRF analysis of rocks from the Miomaffo massif

Conventional Xray fluorescence (XRF) analysis is an accepted technique for the acquisition of accurate and precise lithogeochemical data from bulk samples. However, this and other laboratory-based methods, suffer from high analytical costs. Portable X-ray fluorescence (pXRF) analysers can rapidly and inexpensively provide chemical concentrations of a range of geologically significant elements, often with instrument detection limits below 100 ppm (Ryan *et al.,* 2017).

pXRF analysis was used to assess the chemical composition of the two hundred samples collected in this study (171 from the Mutis Complex). An Olympus Vanta instrument equipped with a rhodium (Rd) X-ray tube anode was used. Analyses were performed in "geochemistry" mode using two beams (40 keV and 10 keV) with 30 seconds of analysis time per beam, Calibration of the equipment was performed using a suite of standard reference materials before, during and after the analyses to correct the data (for each element) as recommended by Fisher *et al.* (2014). The "geochemistry" mode was selected as most suitable for fast screening across a wide range of elements (Lemière 2018). The pXRF method has been used in various geological environments to provide reconnaissance level bulk compositions (eg. Gazley *et al.*, 2011; Jones *et al.*, 2005; McNulty *et al.*, 2018). The analyses are shown in Table 1.

In this study, the analyses were measured on flat surfaces on the samples and carry increased error associated with the small sample size (McNulty *et al.*, 2018). However, most of the rocks are fine grained and the analyses show only moderate dispersion due to sampling error. For example, if we consider the metabasalts in the Mutis Complex, we can compare the high quality conventional XRF analyses to the pXRF of the same samples (Figure 1). The pXRF analyses from these samples show good correlation with the more precise conventional XRF values.
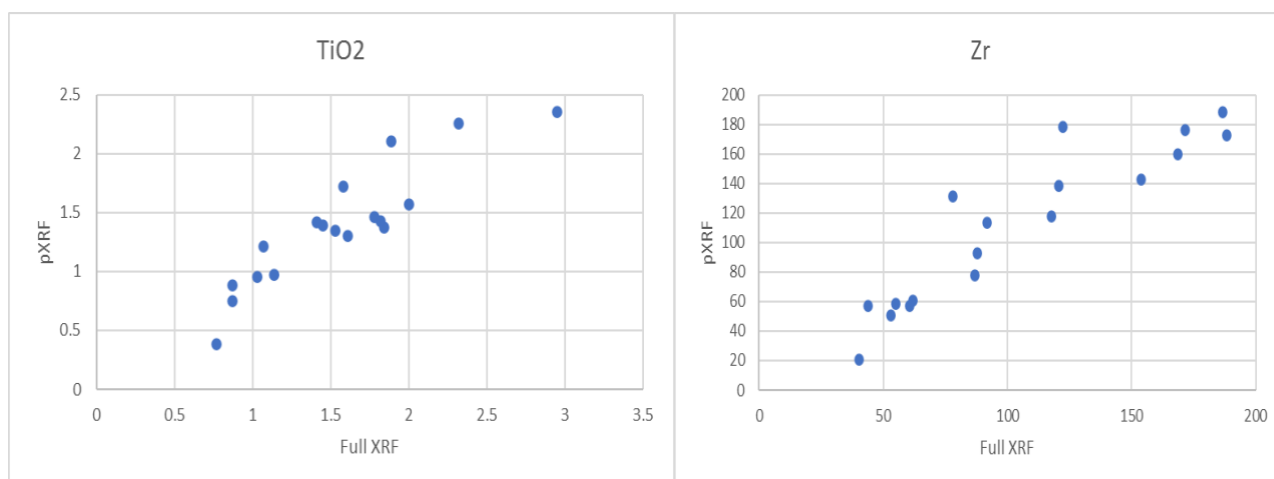

Figure 1. Comparison of pXRF estimates of basaltic
compositions with the same sample measured using conventional XRF techniques (Supplemental data 1) for TiO$_2$ and Zr.

All the metabasalts in the Mutis Complex have immobile element compositions typical of tholeiites. More accurate analysis of the metabasalt compositions is included in Supplemental data 2. The other Mutis Complex rocks are interpreted here as volcaniclastic to epiclastic in origin. The rocks have low SiO$_2$ and high TiO$_2$, FeO, MgO and CaO. The samples from the central and east sector plot in the Fe sand and Fe shale domain of Figure 2. The samples from the western sector are lower in FeO. No compositions typical for pelitic compositions were found. Excluding the siliceous rocks, the samples have too much FeO (average 10%), MgO (average 8%), and CaO (average 7%), and too low a K2O (average 0.8%) for typical pelitic rocks (Figure 4).

On a plot of Zr versus SiO$_2$ (Figure 3) most of the sedimentary rocks have SiO$_2$ typical of basalt. Eight samples have increasing SiO$_2$ at lower Zr reflecting addition of biogenic silica. Three samples have high calcite shown on Figure 3 as a dilution trend towards limestone. There is very little evidence of sorting which should shift the composition to higher SiO$_2$ and Zr. All these rocks have an unusual mafic composition compared to average sedimentary compositions (cf. Taylor & McLennan, 1985).
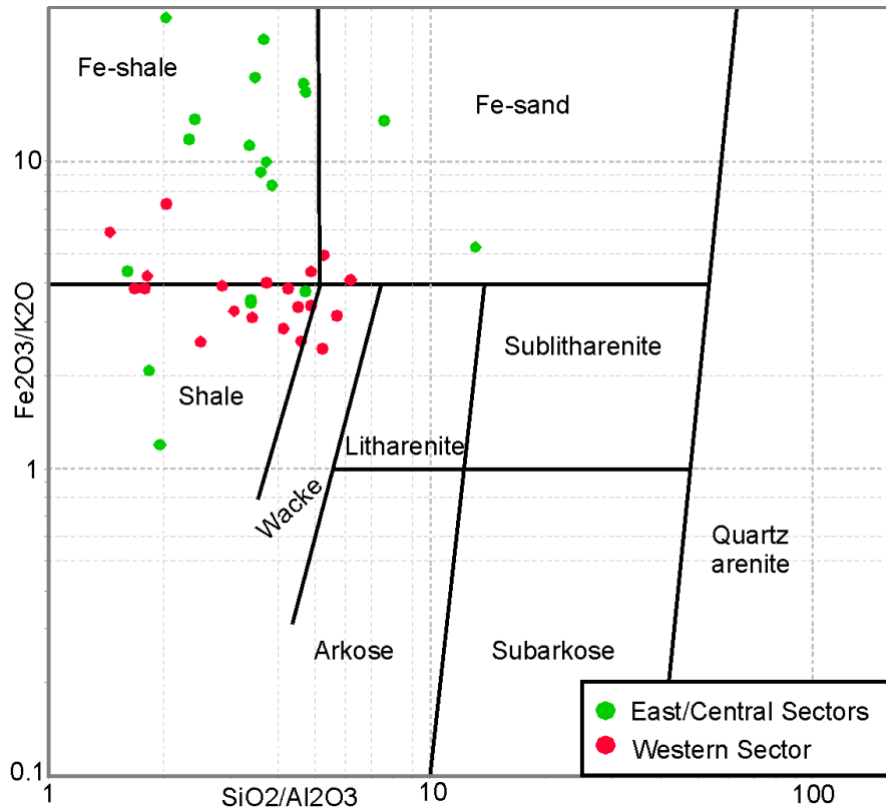
Figure 2. Composition of metasedimentary rocks of the Mutis Complex showing the classification suggested by Herron (1988).
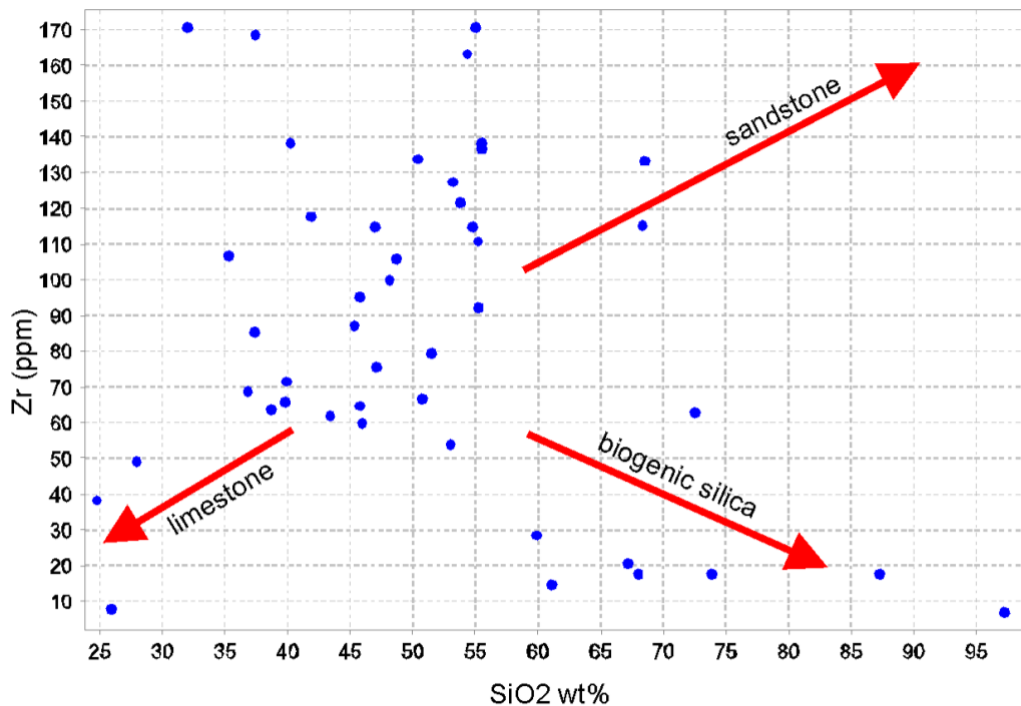

Figure 3. Composition of eastern zone sedimentary rocks showing compositional trends towards siliceous argillite and marl. Analyses are by pXRF.

The average composition of the Mutis Complex volcaniclastic rocks from the eastern and central sector of the Miomaffo massif are very similar to the mafic sands of Colorado and Oregon reported by van de Kamp and Leake (1985). Based of trace elements (Figure 4) these rocks were derived from MORB basalt similar in composition to the blocks of metabasalt in the area (Supplemental data 2). Larue and Sampayo (1990) concluded that sediments of this composition form on oceanic seamounts, rises and plateaus far from continental sources.
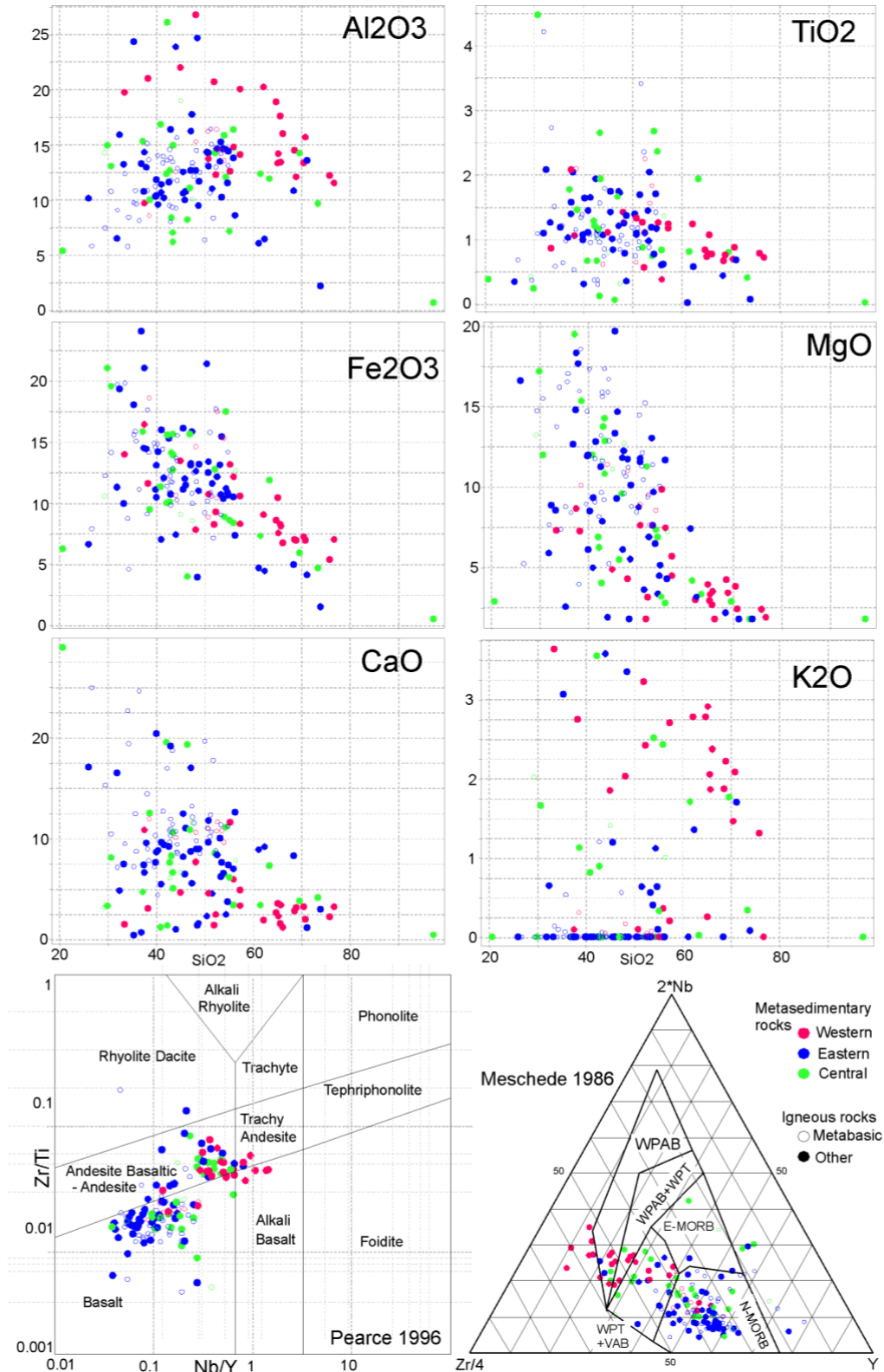

Figure 4. Composition of metasedimentary rocks by pXRF. (metabasic rocks shown in open circles for comparison).

4

In the western section of the Miomaffo massif, some of the garnet gneiss samples have relict volcaniclastic texture. The western sector rocks are also higher in SiO_2 and K2O (Figure 4) than the eastern and central sectors. The western sector rocks have immobile trace elements typical of andesites with island arc chemistry (Figure 4). The composition of the garnet gneiss indicates the western sector rocks have a different provenance from the eastern and central sections, but the detrital zircon U/Pb results (Supplemental data 4) shows they have a very similar age of deposition. There was no evidence of older zircons typical of a continental provenance. They were probably deposited closer to an island arc than the central and eastern sector rocks, and these various lithologies have been juxtaposed in the accretionary prism south of Sundaland. The metamorphic history (Supplemental data 3, 5, 6) demonstrates the final assembly of the Miomaffo massif was after 37 Ma.

References

Fisher, L., Gazley, M. F., Baensch, A., Barnes, S. J., Cleverly, J., & Duclaux, G. (2014). Resolution of geochemical and lithostratigraphic complexity: a workflow for application of portable X-ray fluorescence to mineral exploration. *Geochemistry: Exploration, Environment, Analysis, 14*, 149–159. https://doi.org/10.1144/geochem2012-158

Gazley, M. F., Vry, J. K., du Plessis, E., & Handler, M. R. (2011). Application of portable X-ray fluorescence analyses to metabasalt stratigraphy, plutonic gold mine, Western Australia. *Journal of Geochemical Exploration, 110*, 74–80. https://doi.org/10.1016/j.gexplo.2011.03.002

Herron, M. M. (1988). Geochemical classification of terrigenous sands and shales from core or log data. *Journal of Sedimentary Petrology, 58*, 820–829. https://doi.org/10.1306/212F8E77-2B24-11D7-8648000102C1865D

Jones, M. C., Williams-Thorpe, O., Potts, P. J., & Webb, P. C. (2005). Using Field-Portable XRF to Assess Geochemical Variations Within and Between Dolerite Outcrops of Preseli, South Wales. *Geostandards and Geoanalytical Research, 29*, 251–269. https://doi.org/10.1111/j.1751-908X.2005.tb00899.x

Larue, D. K., & Sampaya, M. M. (1990). Lithic-volcanic sandstones derived from oceanic crust in the Franciscan Complex of California: 'sedimental memories' of source rock geochemistry. *Sedimentology, 37*, 879–889. https://doi.org/10.1111/j.1365-3091.1990.tb01831.x

Lemière, B. (2018). A review of pXRF (field portable X-ray fluorescence) applications for applied geochemistry. *Journal of Geochemical Exploration, 188*, 350–363. https://doi.org/10.1016/j.gexplo.2018.02.006

McNulty, B., Gemmell, J. B., Berry, R., & Fox, N. (2018). Lithological discrimination of altered volcanic rocks based on systematic portable X-ray fluorescence analysis of drill core at the Myra Falls VHMS mine, Canada. *Journal of Geochemical Exploration, 193*, 1–21. https://doi.org/10.1016/j.gexplo.2018.06.005

Meschede, M. (1986). A Method of Discrimination between Different Types of Mid-Ocean Ridge Basalts and Continental Tholeiites with the Nb–Zr–Y Diagram. *Chemical Geology, 56*, 207–218. https://doi.org/10.1016/0009-2541(86)90004-5

Ryan, J. G., Shervais, J. W., Li, Y., Reagan, M. K., Li, H. Y., Heaton, D., Godard, M., Kirchenbaur, M., Whattam, S. A., Pearce, J. A., Chapman, T., Nelson, W., Prytulak, J., Shimizu, K., et al. (2017). Application of a handheld X-ray fluorescence spectrometer for real-time, high-density quantitative analysis of drilled igneous rocks and sediments during IODP Expedition 352. *Chemical Geology, 451*, 55–66. https://doi.org/10.1016/j.chemgeo.2017.01.007

Taylor, S. R., & McLennan, S. M. (1985). *The Continental Crust; Its Composition and Evolution*. Blackwell, Malden, Mass.

Van de Kamp, P. C., & Leake, B. E. (1985). Petrography and geochemistry of feldspathic and mafic sediments of the northeastern Pacific margin. *Transactions of the Royal Society of Edinburgh: Earth Sciences, 76*, 411–449. https://doi.org/10.1017/S0263593300010646

Supplemental data 2. Whole-rock geochemical analyses of basalts and dykes, Miomaffo

Nineteen mafic rocks were analysed for major and trace elements by XRF and ICP-MS at the University of Tasmania (Table 1). The samples include six samples of metabasic rocks from large fault blocks, six samples of metabasic rocks from smaller blocks in the melange, three samples of amphibolite from the Western zone of Eocene metamorphism (Supplemental data 3, 6) and four dykes that crosscut the Eastern (melange) section of the Mutis Complex.

Methods

Rock samples were prepared for analysis by firstly removing weathered surfaces by hammer and splitter, followed by coarse crushing in a steel jaw crusher. A 50–80 g aliquot of this material was then ground in a tungsten-carbide swing mill.

XRF methods

Major and some trace element analyses were obtained using an automated Philips PW1410 X-ray fluorescence spectrometer. Major elements were measured from glass discs prepared with 1.50 g lithium borate flux, 0.02 g lithium nitrate and 0.28 g sample powder (Norrish & Hutton, 1969). Trace elements were measured from pressed powder pills backed by boric acid. Mass absorption coefficients were calculated from the major element composition. Loss-on-ignition was determined by heating 1 g of sample powder to 1000 °C for 12 hours. The analytical precision was 1% relative above 10% absolute and 2% relative for 1–9 % absolute. Zr was measured at 2% relative error above 100 ppm.

Trace elements were measured by ICP-MS methods. The elements analysed were: Li, Be, Sc, Ti, V, Cr, Mn, Ni, Cu, Zn, Rb, Sr, Y, Zr, Nb, Mo, Ag, Cd, Sn, Sb, Te, Cs, Ba, REE (La, Ce, Pr, Nd, Sm, Eu, Gd, Tb, Dy, Ho, Er, Tm, Yb, Lu), Hf, Ta, Tl, Pb, Bi, Th and U. As, Ag and Te were below detection in almost all samples and are not reported. Zr was checked against the XRF result. One sample showed evidence of incomplete zircon dissolution, and this sample was discarded leaving the 19 samples reported here.

Low blank reagents were used for dissolution. All concentrated acids used were Seastar BASELINE high purity grade (Seastar Chemicals Inc, USA). All water used was Type-I Milli-Q ultra-pure water (Merk Millipore). A $HF–H_2SO_4$ High Pressure Digestion Method was applied for complete dissolution of refractory minerals (zircon, chromite, monazite, etc.) (Yu, 2000). The heating was performed in a PicoTrace-GmbH (Germany) high pressure acid digestion system.

Samples were digested in acids at high pressure and temperature. 3 mL HF and 3 mL H_2SO_4 was added to 100.000 ± 0.005 mg of powdered sample in 25 mL PTFE vessels and heated under pressure at 180°C for 24 hours. The acid was then evaporated, to insipient dryness. To remove all trace HF and H_2SO_4, $HClO_4$ was added and again evaporated to insipient dryness. The final residue was dissolved in 2 mL HNO_3 and 5 mL water, by heating to ~70 °C overnight. Samples were then spiked with 10ppb Rh, In and Re as the internal standards and diluted to 100.0 mL (1000 times dilution). The final solutions in an acid matrix of 2% HNO3 were analysed on an Agilent 7700x ICP-MS within 24 hours of dilution. Digestion method blanks and standard referenced materials (SRM) were processed and analysed alongside samples.

Mass-spectral data were collected as counts per second using Mass Hunter (Agilent®) software and reduced through home-developed EXCEL (Microsoft Corporation®) spread sheet. Mid-curve concentration solution and reagent blanks were used to evaluate contamination, precision and accuracy of the analysis. Raw data were corrected by blank contribution, isobaric interferences, and mass drift. Quantification was performed against multi-elemental standard solutions from CHOICE Analytical® and corrected by linear regression on the analysed SRM (TASBAS, TASGRAN and AGV-2).

Results

The 19 samples are from four groups of samples. The six analyses of small basaltic blocks in melange are interpreted as Mesozoic meta-basalts (Table 1) based on field relationships. The six samples of metabasalt (Table 1) from one large basaltic fault block (Figure 1) have similar textures and metamorphic grade to the blocks in melange. Zircon in a pegmatitic patch from this zone indicate a Lower Jurassic crystallisation age (Supplemental data 4). The three amphibolite samples (Table 1) from the western sector are older than the Eocene metamorphism and are probably also Jurassic in age (Supplemental data 3, 4). The four andesitic dykes (Table 1) that crosscut the melange in the eastern sector are younger than 180 Ma (Supplemental data 3) and probably Eocene in age (Harris, 2006).
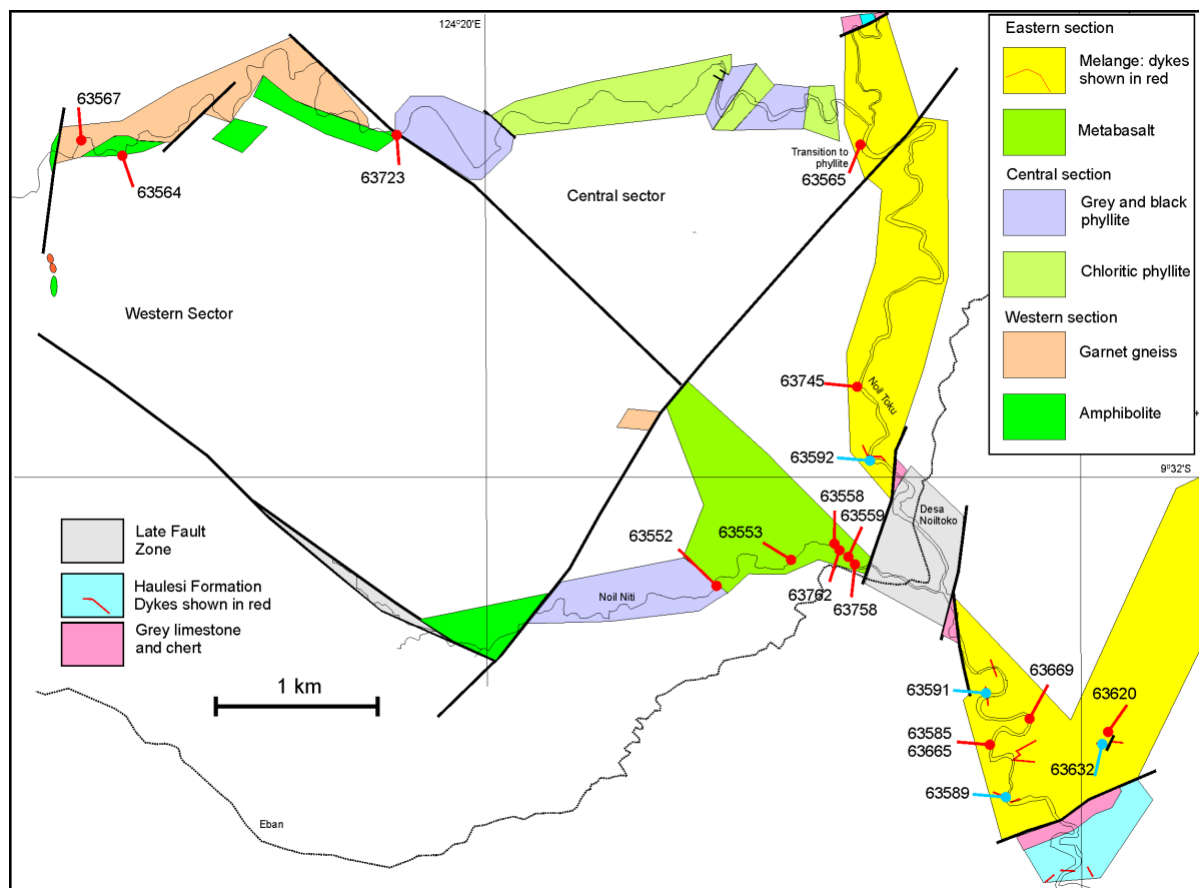
Figure 1. Location of igneous samples. Red symbol for metabasic rocks and blue for andesitic dykes.

Considering only the older mafic rocks (excluding the dykes), all samples have basaltic composition (46–52 wt% SiO_2). The amphibolites have lower SiO_2, more FeO and lower MgO perhaps reflecting a tholeiitic Fe enrichment trend. The more metamorphosed mafic rocks have a flat REE pattern unlike the LREE depleted patterns in most of the other mafic rocks. All the samples plot in the sub-alkaline basalt field of Pearce (1996, figure 2). In most trace-element-classification diagrams they plot in the N-MORB field (e.g., Pearce, 2014, figure 4; Wood, 1980, figure 3). We concluded these are examples of off-scraped ocean floor basalts, formed either at mid-ocean ridge or a backarc spreading centre, collected in an accretionary prism on the southern margin of Sundaland in the Mesozoic.
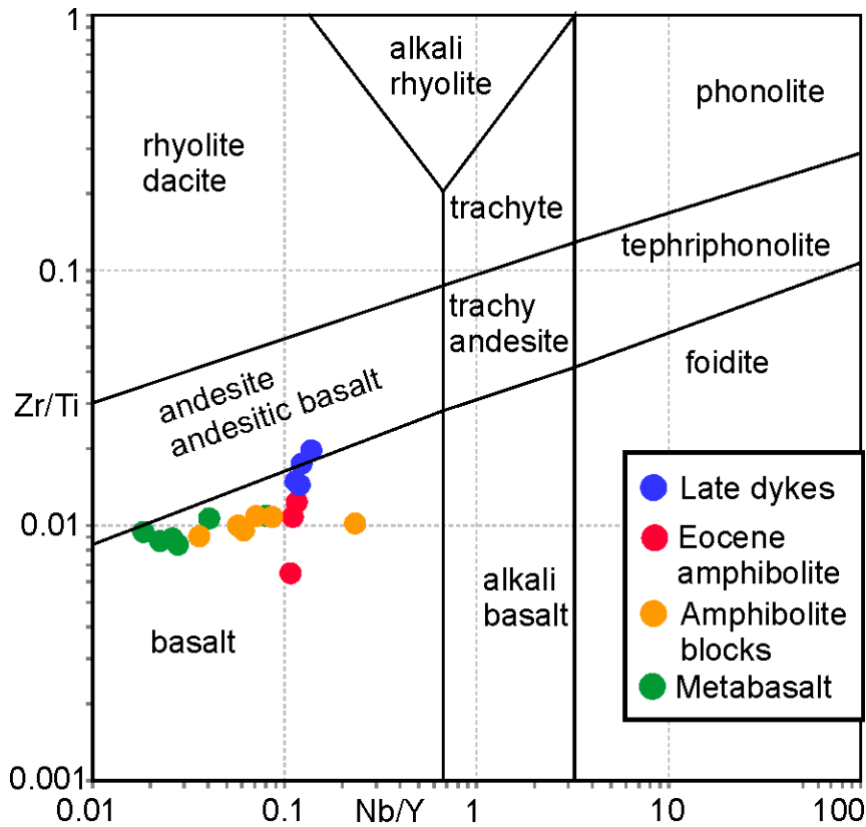
Figure 2. Meta-igneous rocks of the Mutis Complex plotted on the Zr/Ti versus Nb/Y diagram of Pearce (1996). "Amphibolite blocks" includes both greenschist and amphibolite facies blocks in the Eastern sector.
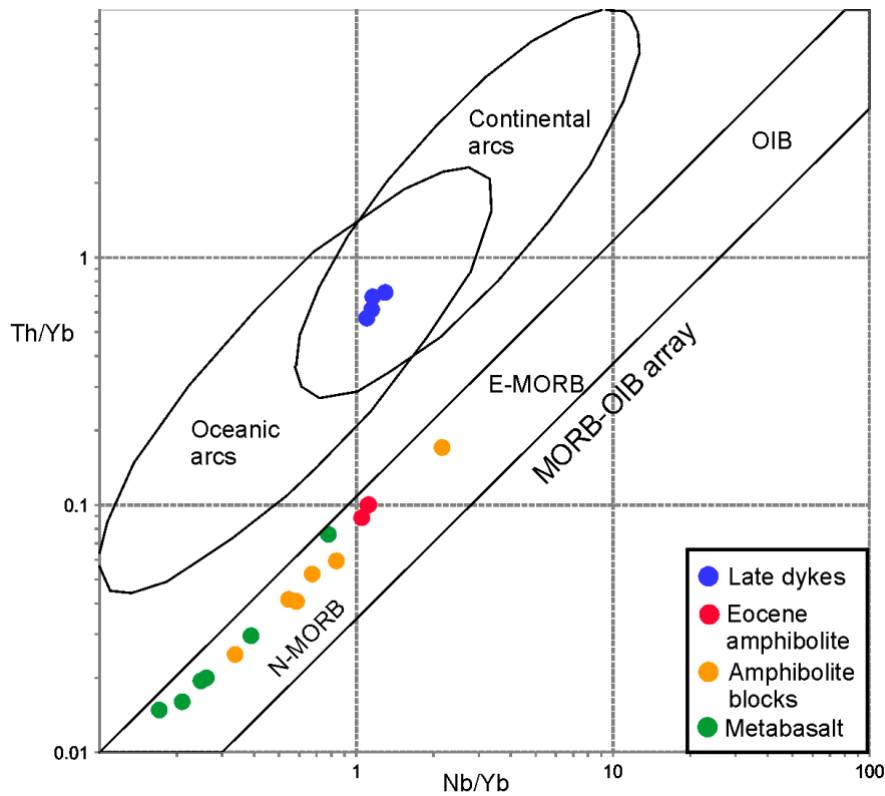

Figure 3. Meta-igneous rocks of the Mutis Complex plotted on the Th/Yb versus Nb/Yb diagram of Pearce (2014)
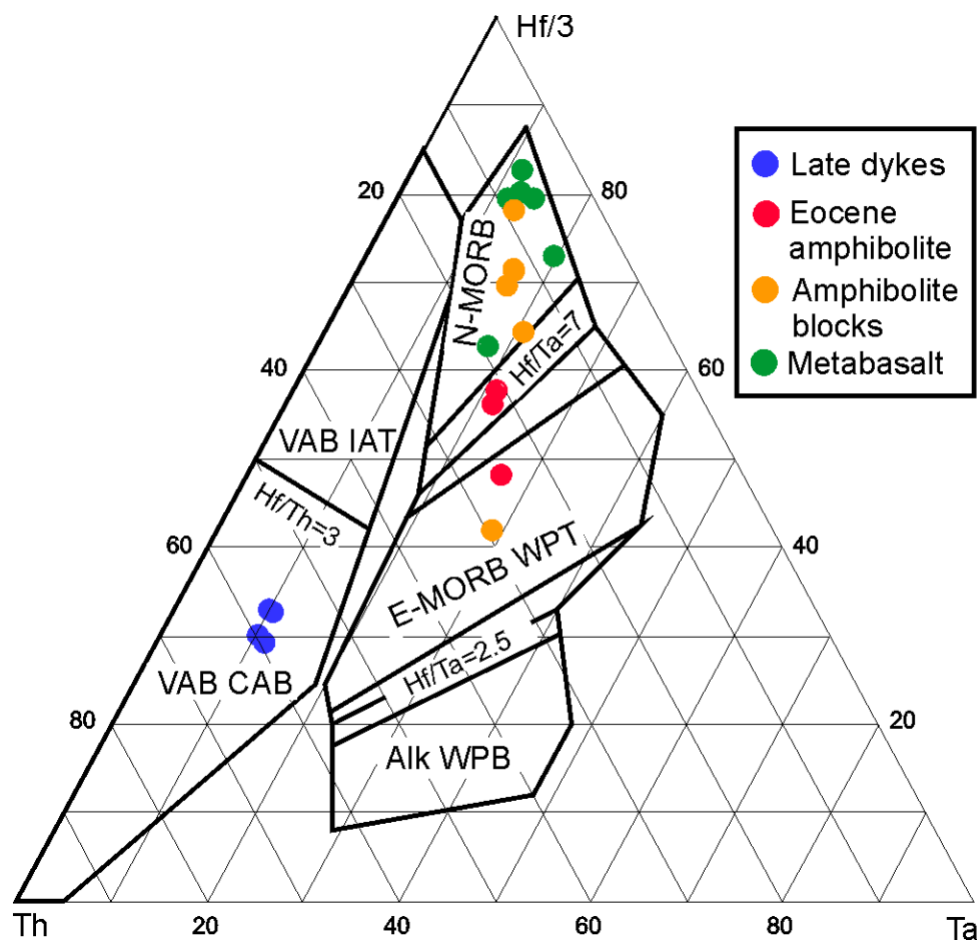
Figure 4. Meta-igneous rocks of the Mutis Complex plotted on the. Th–Hf–Ta diagram of Wood (1980)

Eocene dykes

The four dykes in the eastern melange complex are basaltic andesite to andesite in composition (54–60 wt% SiO_2). The dykes are chemically evolved, as shown by their intermediate SiO_2 contents and low MgO, Ni and Cr abundances (Table 1). They also contain moderately high amounts of TiO_2 and Zr. Their K_2O, Rb and Sr contents are highly variable and their Na_2O concentrations unusually high. These elements have probably been affected by alteration. The REE show a small LREE enrichment trend and a small negative Eu anomaly. In trace element terms the dykes straddle the basalt to basaltic andesite field (Figure 2). They all fall in the arc basalt field of the Th–Hf–Ta diagram (Wood, 1980, figure 3). Chemically they lie in the ambiguous area between continental and oceanic arcs on the Th/Yb vs Nb/Yb field of Pearce (2014, figure 4).

Comparison with Lolotoi suite in East Timor

Park *et al.* (2014) reported a suite of tholeiitic basalt and andesites in the Lolotoi Complex at Forohem, 100 km east of Miomaffo. The Forohem basaltic suite is very similar in composition to the mafic rocks at Miomaffo. They also mainly plot in the N-MORB field for tholeiitic basalts. The andesitic rocks from Forohem are calc-alkaline and Jurassic in age. No correlates for these andesites were analysed from Miomaffo.

Comparison with Sumba

Lytwyn *et al.* (2001) reported the geochemical composition from the Tanadaro volcanic and plutonic suite (*ca* 60 Ma) and the Jawila Volcanics (*ca* 40 Ma). These rocks are from 400 km west of Miomaffo and represent examples of igneous rocks from the forearc south of the Banda Arc. The volcanic rocks on Sumba range from basalts to andesites, and are of typical oceanic island-arc affinity, and generally have medium K calc alkaline compositions. They are unlike the low K tholeiitic series compositions of the Miomaffo dykes.

Discussion

The three suites of metabasalts all have very similar compositions. The large southern fault block may be a larger block in the melange but is grouped here with the Central Sector high strain zone that continues to the

west. This block is Lower Jurassic in age (Supplemental data 4). The smaller blocks in the melange are inferred to also be Mesozoic in age. The detrital zircon inheritance of metasedimentary rocks in the western metamorphic zone also support an early Mesozoic crystallisation age for the metabasalts and amphibolites. On the present information all these rocks could be examples of off-scraped oceanic crust incorporated into an accretionary complex south of Sundaland in the Mesozoic. The dykes are probably Eocene in age (Harris, 2006). Based on this interpretation the absence of dykes from the western metamorphic zone can be interpreted in two ways. The dykes may be slightly older than the preferred age, older than 38 Ma, and thus cannot be recognised after the high strain and medium grade metamorphism in this area, or, if the dykes are younger than 35 Ma, these two blocks were well separated at the time of the intrusions, and only juxtaposed after the andesitic dykes formed.

References

Harris, R. (2006). Rise and fall of the eastern Great Indonesian Arc recorded by the assembly, dispersion and accretion of the Banda Terrane, Timor. *Gondwana Research*, *10*, 207–231. https://doi.org/10.1016/j.gr.2006.05.010

Lytwyn, J., Rutherford, E., Burke, K., & Xia, C. (2001). The geochemistry of volcanic, plutonic, and turbiditic rocks from Sumba, Indonesia. *Journal of Asian Earth Sciences, 19,* 481–500. https://doi.org/10.1016/S1367-9120(00)00031-6

Norrish, K., & Hutton, J. T. (1969). An accurate X-ray spectrographic method for the analyses of a wide range of geologic samples. *Geochimica Cosmochimica Acta, 33*, 431–451. https://doi.org/10.1016/0016-7037(69)90126-4

Park, S-I., Kwon, S., & Kim, S. W. (2014). Evidence for the Jurassic arc volcanism of the Lolotoi complex, Timor: Tectonic implications. *Journal of Asian Earth Sciences, 95*, 254–265. https://doi.org/10.1016/j.jseaes.2014.05.007

Pearce, J. A. (1996). A user's guide to basalt discrimination diagrams. In D. A. Wyman (Ed.) *Trace Element Geochemistry of Volcanic Rocks: Applications for Massive Sulphide Exploration* (pp. 79–113). Geological Association of Canada, Short Course Notes 12,

Pearce, J. A. (2014). Immobile Element Fingerprinting of Ophiolites. *Elements*, 10, 101–108. https://doi.org/10.2113/gselements.10.2.101

Wood, D. A. (1980). The application of a Th Hf Ta diagram to problems of tectonomagmatic classification and to establishing the nature of crustal contamination of basaltic lavas of the British Tertiary Volcanic Province. *Earth and Planetary Science Letters*, *50*(1), 11–30, https://doi.org/10.1016/0012-821X(80)90116-8

Yu, Z. (2000). Development and application of Inductively Coupled Plasma-Mass Spectrometric Techniques for precise measurement of trace elements and lead isotopic compositions in geological materials [unpublished PhD Thesis]. University of Tasmania http://eprints.utas.edu.au/22068/.

Supplemental data 3. Unpublished K/Ar and Ar/Ar data of the Mutis Complex, Miomaffo

Data generated by R. F Berry and I. McDougall (RSES)

Hornblende from four amphibolite samples from the Mutis Complex, Miomaffo were analysed at RSES, ANU in 1984. These included three examples of amphibolite from the western sector and one example of an amphibolite block in the eastern melange (Figure 1).
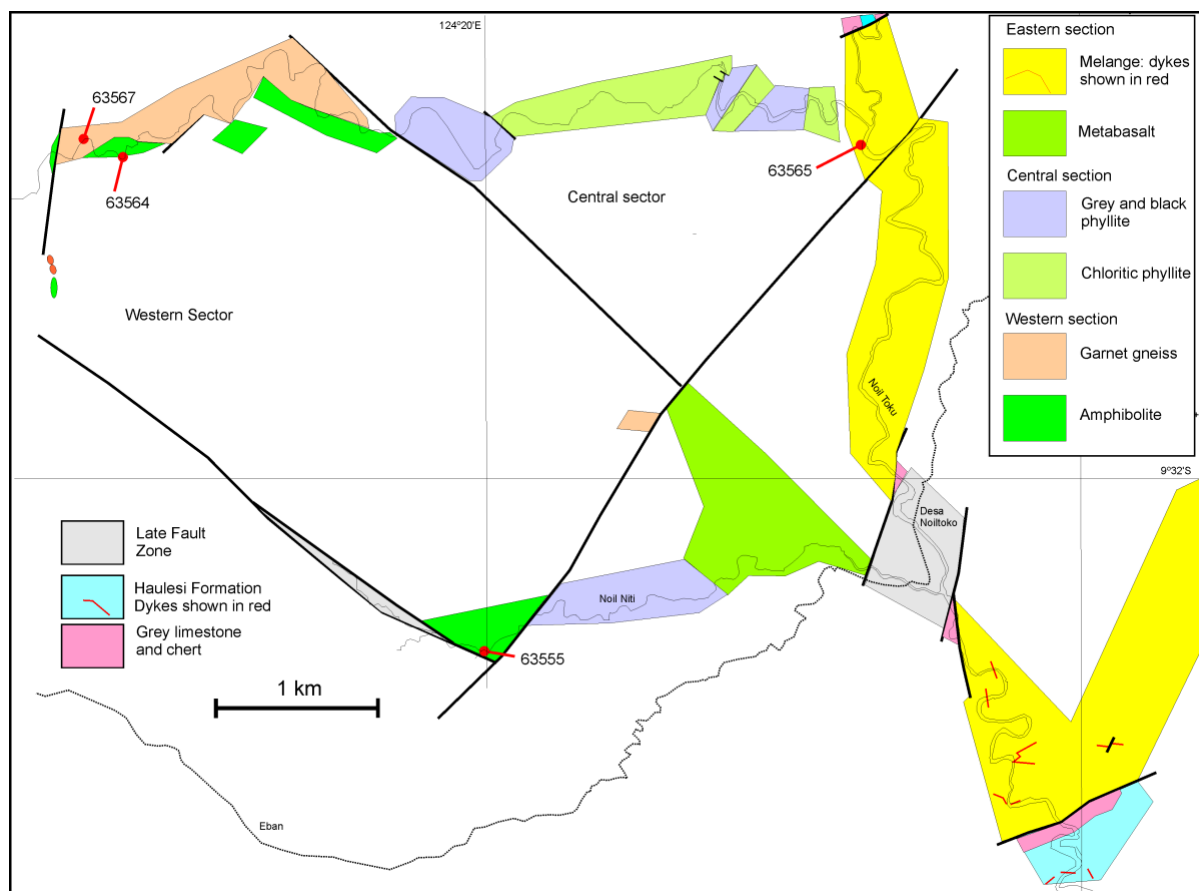

Figure 1. Location of amphibolite samples use for K/Ar and Ar/Ar age dating.

Mineral separates of hornblende were obtained by heavy liquid and magnetic separator techniques. The separates were better than 97% pure. The hornblende separates typically contain 1% plagioclase, 1% sphene and 0.5% ilmenite as inclusions and in composite grains. All samples were separated at particle sizes between 0.25 and 0.12 mm. These samples were subjected to conventional K–Ar dating and three of the samples were analysed by $^{40}Ar/^{39}Ar$ analysis (Merrihue & Turner, 1966). Standard analytical techniques were used, as described by Walker and McDougall (1982). All samples for $^{40}Ar/^{39}Ar$ dating were irradiated for 120 hr in the X33 facility of the Australian Atomic Energy Commission HIFAR@ reactor at Lucas Heights, N.S.W. All K/Ar and Ar/Ar analyses were carried out at RSES.

During Ar extraction, sample temperatures were monitored by a Pt–PtRd,,% thermocouple and an optical pyrometer. The temperatures quoted in Table 2 are precise to ± 10°C within a single run and ± 20°C between samples. The temperature quoted is derived from an average of the two monitored temperatures over the range where they are both accurate (700–950°C), with extrapolations to higher and lower temperatures being made using the thermocouple. The accuracy of these temperatures is ± 50°C. The Ar isotopic analyses for K/Ar dating were done in an AEI@ MS10 mass spectrometer. The isotopic composition of Ar extracted in each step in the $^{40}Ar/^{39}Ar$ study was measured using a VG-Isotopes@ MM1206 mass spectrometer.

Three samples (63555, 63564, 63567) of the Western Sector have a consistent K/Ar age near 40 Ma. Two of these samples were also analysed by $^{40}Ar/^{39}Ar$ methods (Table 1). These samples have poor plateau ages of 36 Ma and 38 Ma (Figure 2). Since the age spectra of both samples show a slight saddle shape the inverse concordia ages of 35.7 ± 1.1 Ma and 37.1 ± 0.4 Ma are preferred here. These ages are very similar

to metamorphic ages recorded from other Mutis Complex blocks ranging from 38–31 Ma (Harris, 2006). The U–Pb apatite age for the western sector (Supplemental data 6) is consistent with the Ar/Ar age dating of this block and other medium to high grade metamorphic blocks in West Timor. However, all the West Timor metamorphic blocks have hornblende Ar ages younger than the 45 Ma. Lu–Hf garnet age reported for the Lolotoi Complex, East Timor (Standley & Harris, 2009).

One sample of a metamorphic block from the eastern melange (63565) has a K/Ar age of 177 Ma (Table 3). The ^{40}Ar/^{39}Ar analysis of this sample was compromised as a one heating step was lost. The ^{40}Ar/^{39}Ar total fusion age of 174.5 ± 2.6 Ma and the isochron age of 184 ± 6 Ma support the Jurassic K/Ar hornblende estimate of the metamorphic age. The isochron age is accepted here as the most reliable age for this sample. This age is consistent with the zircon age for a pegmatitic patch in the host basalts of 200 Ma and the presence of 200 Ma detrital zircon in schist blocks in the melange (Supplemental data 4). It also matches the field relations that indicate the melange is older than Eocene dykes and "unconformably" overlain by Cretaceous sedimentary rocks (Harris, 2006).

The Ar/Ar age dating from the Miomaffo Block indicates that the metamorphic blocks in the melange are much older than the regional metamorphism of the Western Sector of the Miomaffo block.

References

Harris, R. (2006). Rise and fall of the eastern Great Indonesian Arc recorded by the assembly, dispersion and accretion of the Banda Terrane, Timor. *Gondwana Research*, *10,* 207–231. https://doi.org/10.1016/j.gr.2006.05.010

Ludwig, K. R. (2008). User's manual for Isoplot 3.6, a geochronological toolkit for Microsoft Excel. Berkeley Geochronology Center.

Merrihue, C. M., & Turner, G. (1966). Potassium argon dating by activation with fast neutrons. *Journal* of *Geophysical Research*, *71,* 2852–2857. https://doi.org/10.1029/JZ071I011P02852

Park, S.-I., Kwon, S., & Kim, S. W. (2014). Evidence for the Jurassic arc volcanism of the Lolotoi Complex, Timor: tectonic implications. *Journal of Asian Earth Sciences, 95*, 254–265. https://doi.org/10.1016/j.jseaes.2014.05.007

Standley, C., & Harris, R. A. (2009). Banda forearc basement accreted to the NW Australian continental margin: a geochemical, age and structural analysis of the Lolotoi metamorphic complex of East Timor. *Tectonophysics 479,:*66–94. https://doi:org/10.1016/j.tecto.2009.01.034

Walker, D. A., & McDougall, I. (1982). ^{40}Ar/^{39}Ar and K–Ar dating of altered glassy rocks: the Dabi Volcanics, P.N.G. *Geochimica Cosmochimica Acta*, *46*, 2181–2190. https://doi.org/10.1016/0016-7037(82)90193-4
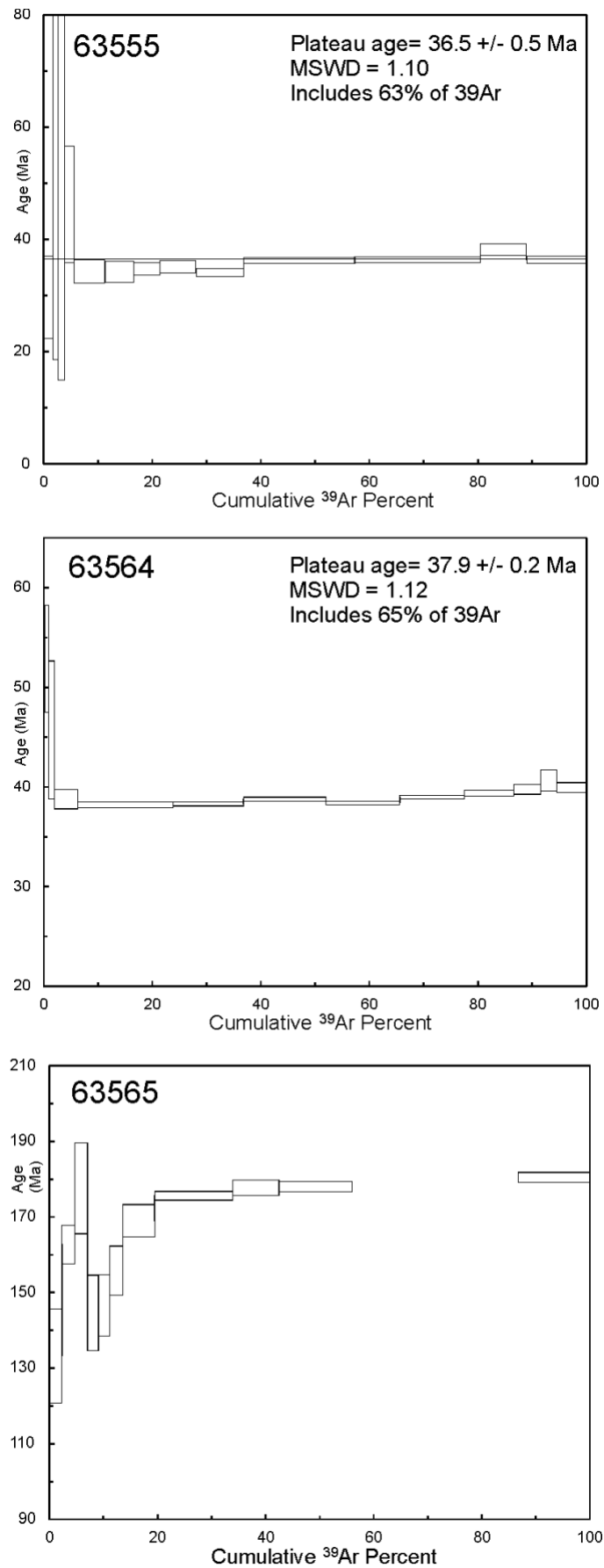
Figure 2. Ar/Ar step heat diagrams for samples from Miomaffo area. Drawn using Isoplot (Ludwig, 2008).

Supplemental data 4. U/Pb Zircon age data for three samples from the Mutis Complex, Miomaffo

Introduction

Zircon is a common detrital mineral that records the maximum depositional age in low grade metamorphic rocks (Vermeesch, 2021) and more rarely can be found in basaltic rocks (Sack *et al.*, 2007). Three samples of pegmatitic patches in metabasalt and two samples of schist from the Mutis Complex were selected for investigation.

Figure 1. Pegmatitic patch in metabasalt.

Conventionally, zircon grains are found by crushing the sample, separating the non-magnetic heavy mineral fraction, and hand picking the grains. However, grains smaller than 30 μm are best analysed *in situ* eliminating the potential for laboratory contamination, preserving the original crystal shapes and providing a geological context for the growth of the crystal (Simonetti *et al.*, 2006). In this project, each sample, a 2 cm rock chip, was encased in a 2.5 cm round epoxy mount, polished and carbon-coated. The zircon grains in these samples were found using a FEI Quanta 600 scanning electron microscope (SEM) with a combination of backscattered electron (BSE) mapping to identify high mean atomic number grains and energy dispersive X-ray spectroscopy (EDS) to identify zircon (Sack *et al.*, 2011). Of these five samples, both of the schist samples had relatively uniform 20 μm zircon grains and one of the metabasalts had three grains of euhedral zircon.

The zircon grains were analysed by laser-ablation induction-coupled-plasma mass spectrometry (LA-ICP-MS). The analyses were carried out using a Resonetics (now ASI) Resolution S-155 ablation system with a Coherent Compex Pro 110 excimer laser operating with ArF to produce wavelength at 193 nm and a pulse width of ~20 ns. All ablations were performed in a He atmosphere and the He gas was blended with Ar immediately outside the sample chamber (Eggins *et al.*, 1998; Jackson *et al.*, 2004; Thompson *et al.*, 2018). ~1.6 mL/min N_2 gas was also added after the ablation cell to increase instrument sensitivity. Laser analytical parameters were similar to those described by (Halpin *et al.*, 2014; Thompson *et al.*, 2018). The Agilent 7900 was tuned to optimise counts and to minimise oxide and doubly charged ion production (ThO/Th<0.15%, Ca^{2+}/Ca<0.5%) after warming up for 2 hours. All analyses were carried out in a single session. The ICP-MS data were processed using the method outlined in Halpin *et al.* (2014). The laser conditions were 5 Hz pulse rate, 13 μm spot size, 2 J cm^{-2} fluence, 30 s gas blank and followed by 30 seconds of ablation. The four

isotopes of Pb, ^{238}U, ^{232}Th, ^{31}P, ^{140}Ce, ^{172}Yb and ^{202}Hg were measured on all spots. The zircon 91500 (Wiedenbeck *et al.*, 1995) was used as the primary calibration standard for Pb/U and Pb/Th isotopes ratios and the NIST 610 glass was used to calibrate the Pb isotopic ratios and the trace elements. See Thompson *et al.* (2018) for a more detailed methodology and discussion of the accuracy and precision. A variety of secondary standards were also analysed to check the calibrations. The time-resolved signal for each laser ablation analysis was examined in detail and the isotopic ratios were calculated on the parts of the signal with low ^{207}Pb/^{206}Pb ratios. Typically, only part of the 30s of data collected from the zircon crystals was used, with the remainder of the analysis ablating mixtures of the zircon and other minerals. Analyses which ablated through the zircon very quickly (<3s) were rejected. The full table of measured ratios is provided in the Table 1. Uncertainties for individual analyses as quoted in tables and as error bars on U–Pb plots have been calculated to the one-sigma level. Weighted mean and intercept ages are reported at 95% confidence limits.

Results

Zircon was found in one pegmatitic patch in metabasalt (63700) but the other two metabasalt samples were barren. Both samples of schist had zircons. These include a schist block within the eastern melange (63580) and in a schist sample from the western metamorphic zone (63725) as shown in Figure 1.

The sample 63700 is of a pegmatitic patch in a metabasalt from the low-grade central section of the area. The sample is 40% amphibole (hornblende and actinolite), 25% albite, 10% clinozoisite and 4% diopside (Figure 3a). Strain in this rock is low but metamorphic reactions have modified the mineral composition. Rare phase search identified 3 zircon grains in a polished block of which the best preserved was 150 m long euhedral grain (Figure 3b).
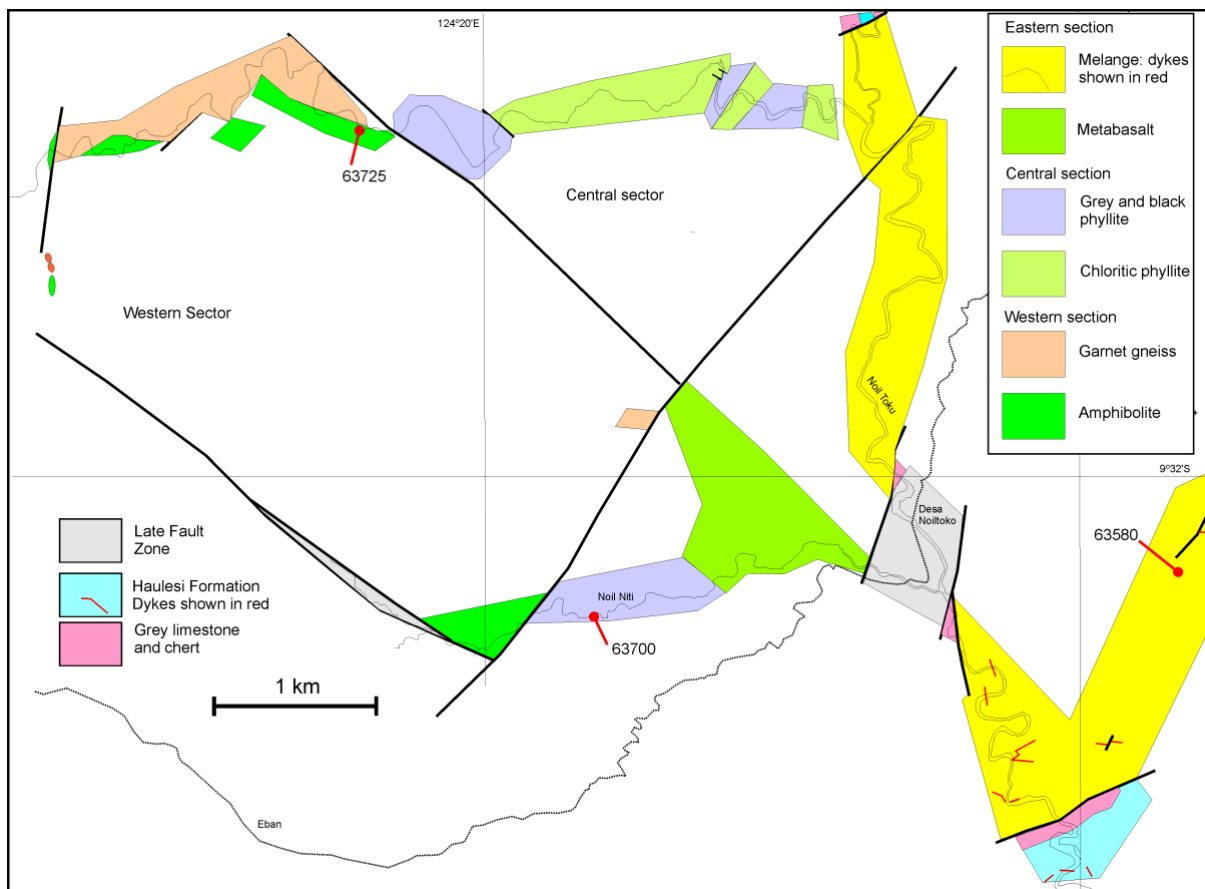

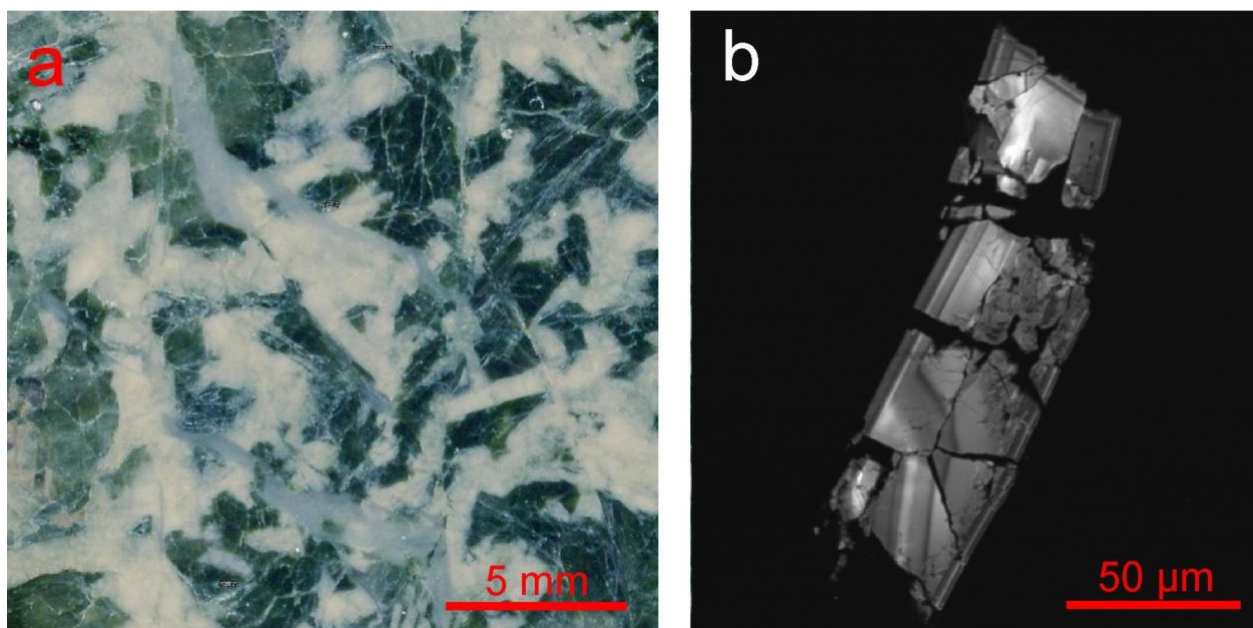*Figure 2. Locations of samples with zircon analysed by LA-ICPMS.*

Figure 3. Texture of pegmatitic patch in metabasalt. (a) Oblique illumination reflected light image. (b) Cathodoluminescent image of zircon grain.

The zircon grains were analysed by LA-ICP-MS. From 11 spot analyses, several had evidence of Pb loss and contamination. The six best concordant analyses gave a consistent age of 194 ± 5 Ma (Figure 4). The preferred age for the basaltic rocks in the Miomaffo Complex is Lower Jurassic.
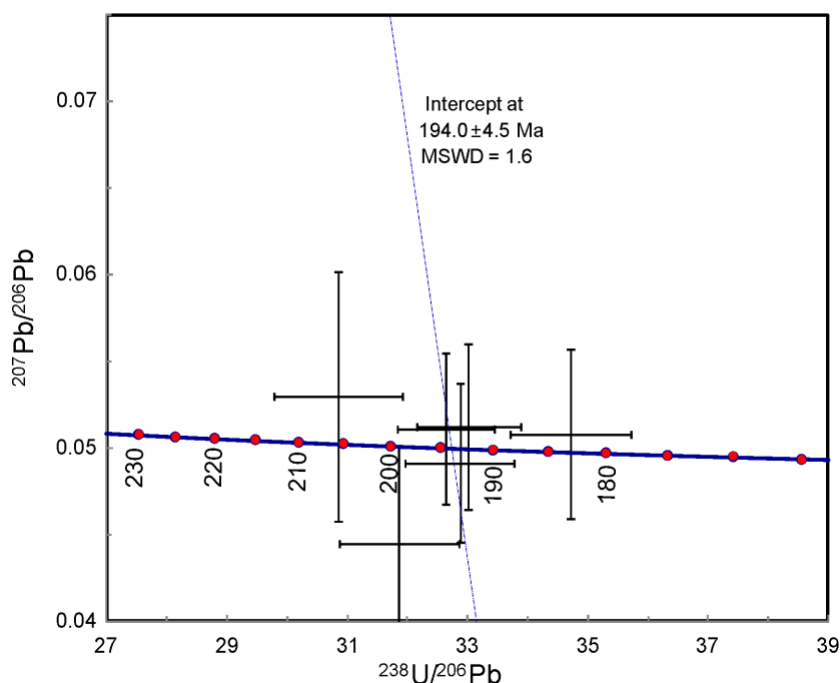

Figure 4. Inverse concordia diagram for zircon analyses on 63700. One sigma error cross shown for each point. Diagram drawn using Isoplot (Ludwig, 2008).

Sample 63580 is an amphibolite facies garnet biotite muscovite schist (see Supplemental data 5). It comes from a large block (50 m across) in the melange that dominates the Eastern Sector of the Mutis Complex at Miomaffo. The sample is higher in SiO_2 and K_2O than the melange matrix. The rare phase search found 100 grains of zircon in the range 10–20 μm diameter. Some grains are broken (Figure 5b) and many have of narrow overgrowths of metamorphic zircon (Figure 5a) but all show magmatic growth zoning in the cores.
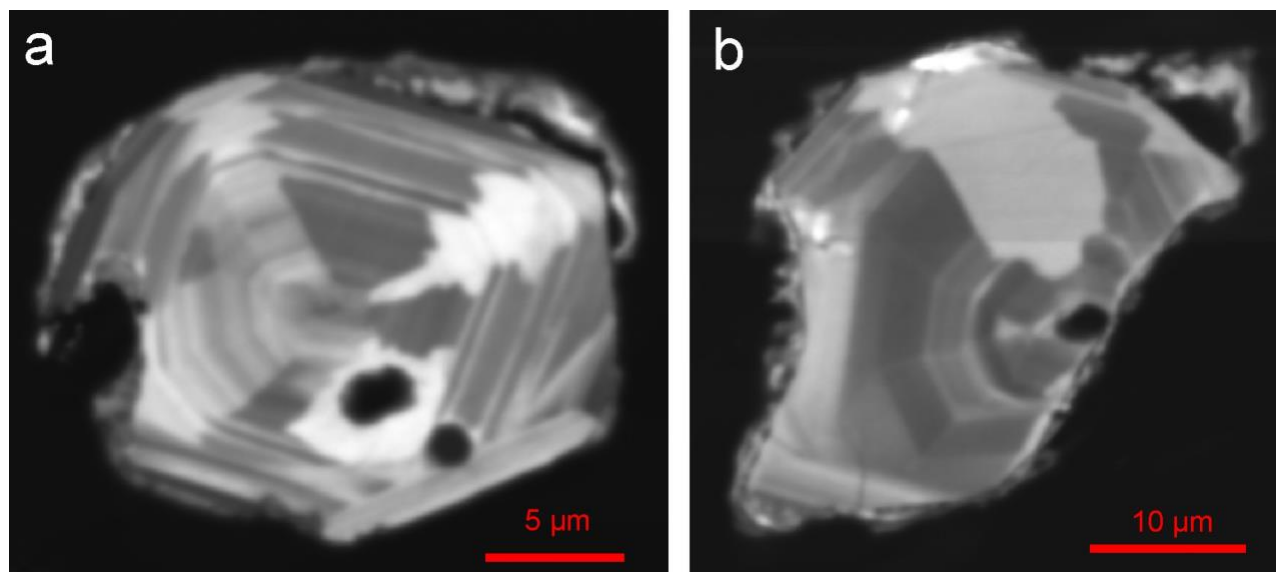
16

Figure 5. Cathodoluminescent images of zircon in sample 63580. (a) Grain showing a euhedral shape with very thin overgrowths of metamorphic zircon. (b) Broken grain with thin overgrowths of metamorphic zircon.

From the 13 analyses that were carried out, many show evidence of Pb loss or contamination. The four best concordant analyses gave a consistent age (Figure 6) of 201 ± 4 Ma. These grains reflect the maximum deposition age for the sandstone. The depositional age must be older than the amphibolite facies metamorphism of the block (probably 184 ± 6 Ma by analogy with the amphibolite sample analysed by Ar/Ar hornblende, see Supplemental data 3). The melange must be Jurassic or younger. There is no evidence in the zircon U/Pb ages measured of a continental provenance for this rock.
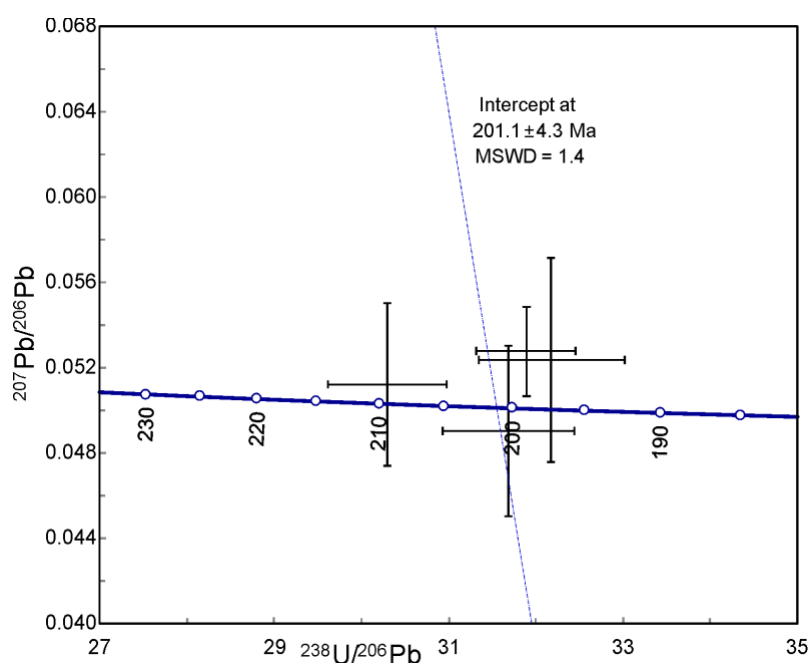

Figure 6. Inverse concordia diagram for zircon analyses on 63580. One sigma error cross shown for each point. Diagram drawn using Isoplot (Ludwig, 2008).

Sample 63725 is a garnet staurolite gneiss from the Western Sector of the Miomaffo massif. It also contains very large apatite grains with a Cenozoic U/Pb age (Supplemental data 6). The metamorphic age of the Western sector is about 37 Ma (Supplemental data 3). The peak metamorphic temperature was 650 ºC (Supplemental data 5) and below the closure temperature for zircon but zircon recrystallisation at high strain

can reset the U/Pb systematics (Oriolo *et al.*, 2018). As with 63580, the rare phase search found more than 100 grains of zircon in the range 10–20 µm diameter. However, CL imaging (Figure 7) showed that many grains had extensive metamorphic rims around a core with complex growth zoning typical of magmatic zircons (Figure 7c).
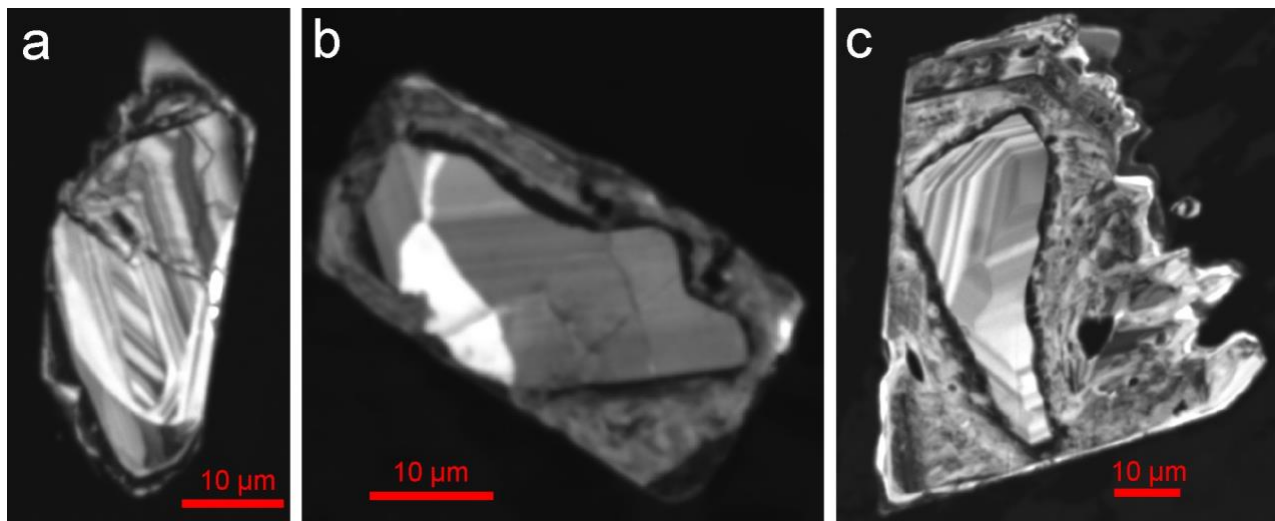

Figure 7. Cathodoluminescent images of zircon in sample 63725. (a) Grain largely showing a magmatic growth zoning with very thin overgrowths of metamorphic zircon. (b) Broken grain with moderate overgrowths of metamorphic zircon. (c) Small core of complexly zoned zircon surrounded by an extensive rim of metamorphic zircon.

Many of the analyses of the zircon grains showed evidence for zoning, presence of common Pb, and Pb loss (Figure 8). The three oldest concordant grains provided a crystallisation age of 194 ± 6 Ma. This is very close to the U/Pb age of detrital zircons founded in sample 63580. The other grains are variably reset to younger ages (Figure 8) with the youngest cluster around 80 Ma. Given the CL images we interpret this variation as mixed ages between the original crystallisation age and the age of the metamorphic zircon rims. The small size of grains and narrow rims means no examples of purely metamorphic zircon age was measured. The preferred age of the metamorphic rims is 37 Ma as determined by the Ar/Ar hornblende analyses (Supplemental data 3).
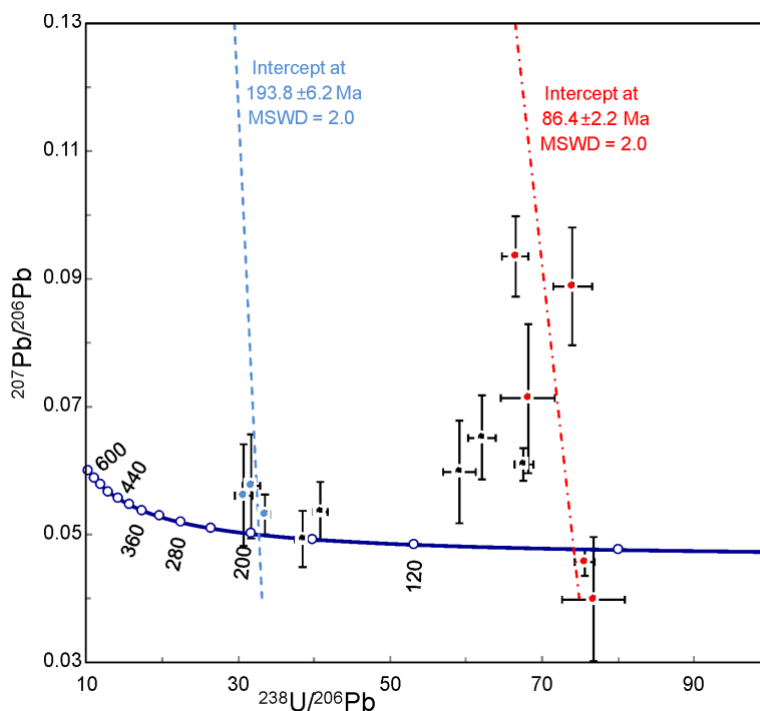

Figure 8. Inverse concordia diagram for zircon analyses in sample 63725. One sigma error cross shown for each point. Diagram drawn using Isoplot (Ludwig, 2008).

Conclusion

The metabasalts in the southern part of the Central Sector formed in the Lower Jurassic. Other meta-sedimentary rocks were sourced from volcanic terranes also of Lower Jurassic age. The melange was assembled after 177 Ma based on the metamorphic age of amphibolite blocks (Supplemental data 3). The Western Sector metamorphism occurred after 80 Ma based on the partially recrystallised zircons in sample 63725.

References

Halpin, J. A., Jensen, T., McGoldrick, P., Meffre, S., Berry, R. F., Everard, J. L., Calver, C. R., Thompson, J., Goemann, K., & Whittaker, J. M. (2014). Authigenic monazite and detrital zircon dating from the Proterozoic Rocky Cape Group, Tasmania: Links to the Belt-Purcell Supergroup, North America. *Precambrian Research*, *250*, 50–67. https://doi.org/10.1016/j.precamres.2014.05.025

Ludwig, K. R. (2008). User's manual for Isoplot 3.6, a geochronological toolkit for Microsoft Excel. Berkeley Geochronology Center.

Oriolo, S., Wemmer, K., Oyhantcabal, P., Fossen, H., Schulz, B., & Siegesmund, S. (2018). Geochronology of shear zones – a review. *Earth Science Reviews, 185*, 665–683. https://doi.org/10.1016/j.earscirev.2018.07.007

Sack, P. J., Berry R. F., Meffre, S., Falloon, T. J., Gemmell, J. B., & Friedman, R. M. (2011). In situ location and U–Pb dating of small zircon grains in igneous rocks using laser ablation–inductively coupled plasma–quadrupole mass spectrometry. *Geochemistry, Geophysics, Geosystems, 12,* Q0AA14. https://doi.org/10.1029/2010GC003405

Simonetti, A., Heaman, L. M., Chacko, T., & Banerjee, N. R. (2006). In-situ petrographic thin section U–Pb dating of zircon, monazite and titanite using laser ablation-MC-ICP-MS. *International Journal of Mass Spectrometry*, *253*, 87–97. https://doi.org/10.1016/j.ijms.2006.03.003

Thompson, J. M., Meffre, S., & Danyushevsky, L. (2018). Impact of air, laser pulse width and fluence on U–Pb dating of zircons by LA-ICPMS. *Journal of Analytical Atomic Spectrometry*, *33*(2), 221–230. https://doi.org/10.1039/C7JA00357A

Vermeesch, P. (2021). Maximum depositional age estimation revisited. *Geoscience Frontiers*, 12, 843–850. https://doi.org/10.1016/j.gsf.2020.08.008

Wiedenbeck, M. A. P. C., Alle, P., Corfu, F., Griffin, W. L., Meier, M., Oberli, F. V., ... & Spiegel, W. (1995). Three natural zircon standards for U-Th-Pb, Lu-Hf, trace element and REE analyses. *Geo-standards Newsletter*, *19*(1), 1–23. https://doi.org/10.1111/j.1751-908X.1995.tb00147.x

Supplemental data 5. Metamorphic history of the Mutis Complex, Miomaffo

The metamorphic grade of the Mutis Complex was estimated using a range of criteria including analysis of mineral chemistry using an electron probe microanalysis (EPMA). The mineral compositional analysis included 10 elements acquired on a JEOL JXA-8530F Plus electron microprobe, equipped with 5 tuneable wavelength dispersive spectrometers, at the CSL, University of Tasmania. Zn was below detection limit except in staurolite where it was 0.4–1.6 wt%. The metamorphic history is discussed separately for each of the three sectors. This section uses the mineral abbreviations of Whitney and Evans (2010) in tables and figures. Sample locations are shown in Figure 1. Mineral analyses are shown in Table 1
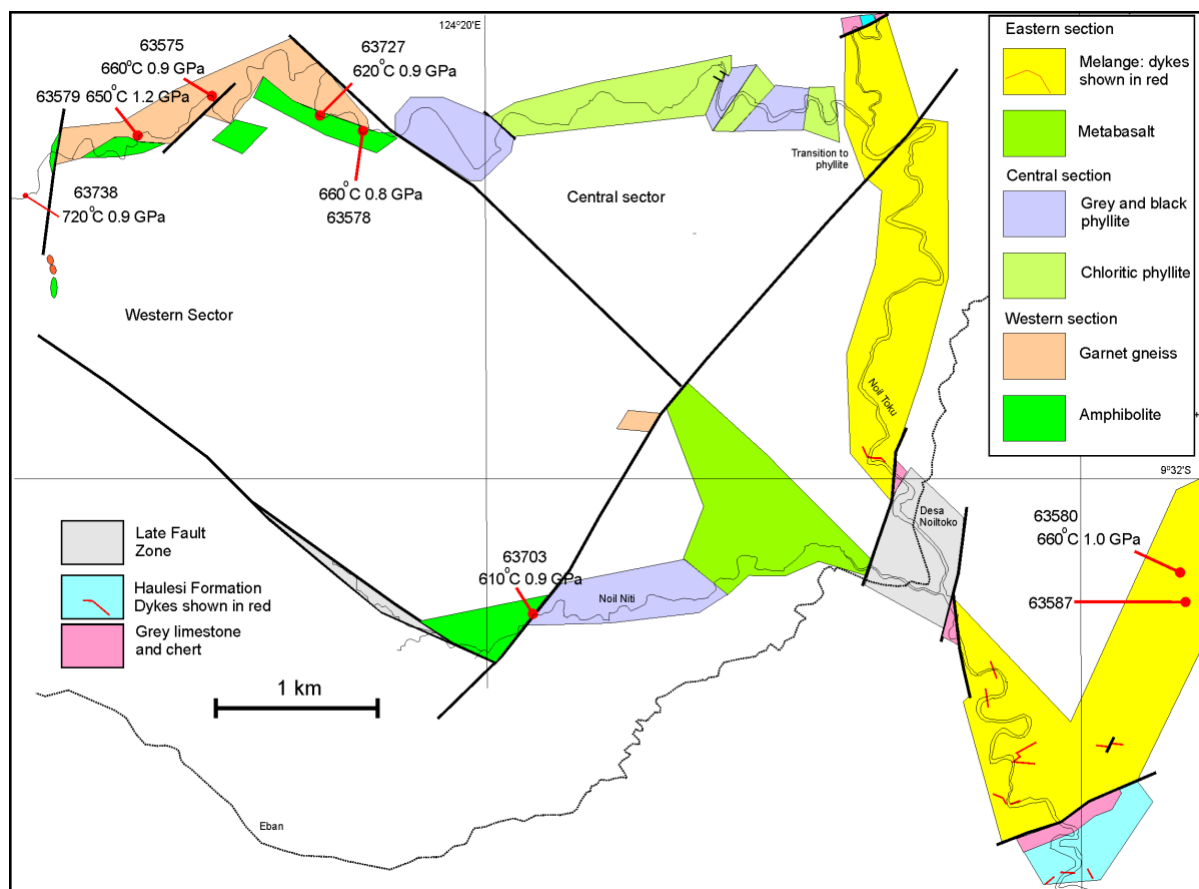

Figure 1. Locations of sample mentioned in Supplemental data 5. Geology shown along mapped traverses.

Eastern Sector

The most common rocks of the eastern sector are the melange matrix and associated metabasic rocks. The metabasic rocks are typically actinolite albite epidote titanite. The mafic volcaniclastic rocks have some quartz, and prehnite is locally visible. Many rocks contain relict igneous augite and calcic plagioclase. Leucoxene is common.

Most of the blocks in the accretionary complex are very low grade with generic low greenschist facies assemblages. A few blocks in the melange have mineralogy consistent with higher metamorphic grade. These include both amphibolite and garnet schist. No blueschist or eclogite blocks were found.

One example of an amphibolite block is 63587, which contains the assemblage hornblende plagioclase chlorite epidote ilmenite titanite. The amphibole is all hornblende with Al_2O_3 varying from 6.5 to 12.3 wt% (Table 1). The plagioclase is An18 (16–20). The temperature of metamorphism calculated using the hornblende plagioclase thermometer of Holland and Blundy (1994) is 700 ºC assuming medium P/T.

An example of a quartz–biotite–garnet schist is 63580. The biotite is extensively chloritised. The compositions of other minerals are shown in Table 1.

The garnet has relatively Mn-rich cores (Figure 2). However, the Ca and Mg number (Mg/Mg+Fe) are relatively constant suggesting very little change in P–T conditions during garnet growth. Using the rim garnet composition and the most common plagioclase composition (An$_{22}$), the average P–T was calculated using Thermocalc (Holland & Powell, 2011) as 660 ± 30º C, 1.0 ± 0.1 GPa, cor. 0.86.
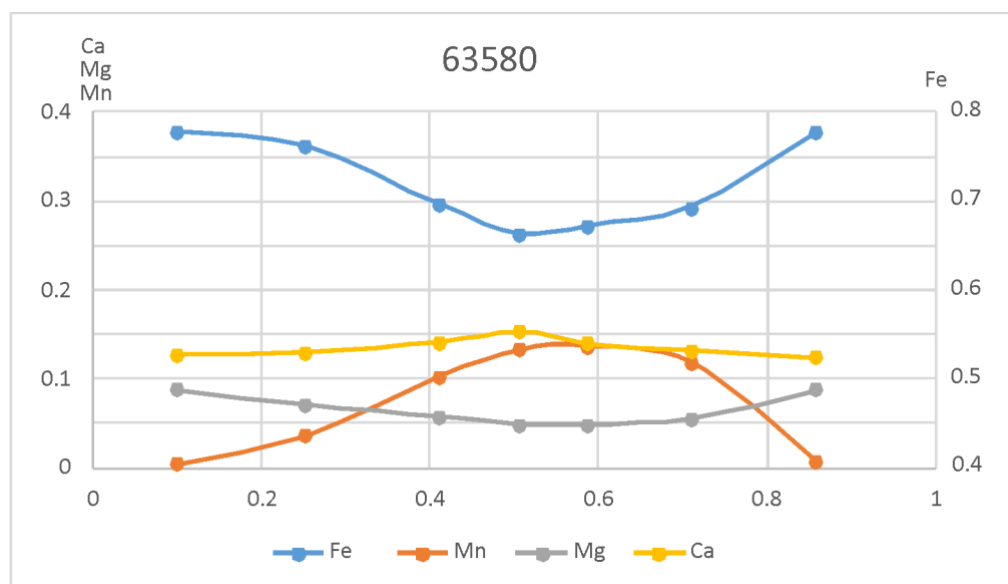

Figure 2. Compositional zoning in garnet from 63580. All elements shown as cations based on 12 oxygens. Note scale for Fe cations is shown on right side. Horizontal axis is in mm.

Central Sector

The central sector has typical greenschist facies assemblages. The most common green rocks have the assemblage epidote, actinolite–albite–chlorite with minor titanite and carbonate, with stilpnomelane in a few samples. The darker rocks are quartz–albite–muscovite ± biotite. Many rocks are clay altered but it is not clear how much of this is due to weathering, and whether any clay alteration is older.

Western Sector

The western side of the Miomaffo Complex is composed of amphibolite grade schist and gneisses. These include similar bulk compositions to those seen further east with slightly higher K and SiO2 in some gneisses. The mineralogy of the amphibolite samples is hornblende plagioclase titanite epidote with minor quartz.

The garnet bearing gneisses have the mineral assemblage: quartz–plagioclase–biotite–staurolite–ilmenite ± margarite, ± paragonite. Sopaheluwakan *et al.* (1989) reported zoning in the gneisses from chlorite zone in the southeast to staurolite zone in the west. To test this samples were chosen from across the area of the gneiss outcrop (Figure 3). Sample 63703 should be chlorite grade according to the map in Sopaheluwakan *et al.* (1989). The other four samples all come from the staurolite zone along the Noil Noni. Sample 63738 comes from farthest west and has a different texture reflecting an early high strain history. Several samples selected for detailed study were first checked for modal composition using SEM point counting (Table 2). This identified some substantial differences. Sample 63725 has large apatite porphyroblasts (see Supplemental data 6). Associated with this high P content, this sample is also much richer in quartz than other samples. Sample 63727 was identified as having margarite (Ca white mica). Margarite is relatively rare but has been identified in other amphibolite facies gneisses in rocks with very high Ca/(Ca+ Na) (Kohn and Spear 1993). Sample 63578 has trace amounts of paragonite that was only detected during EPMA. The chlorite is a common retrograde mineral

Sample 63578 has relatively small garnet and rare staurolite. The garnet has heavily included cores and clear rims. The rocks are very plagioclase rich. The biotite and muscovite contents are less than 5%. Garnet forms as small crystals in clusters (Figure 3). The biotite and muscovite define a foliation that has be tightly folded and then crenulated. The textural evidence is ambiguous, but no evidence was found that the garnets predate the foliation or the weak crenulations. The garnet growth appears to be late.

The garnet grains are small (<1 mm, Figures 3 and 4). The cores have relatively uniform Ca and Mg content, but the clear rims are higher in Mg and lower in Ca (Figure 4). Using the rim compositions in Thermocalc v3.25 (Holland & Powell, 2013) the average P–T is given as 660 ± 20 ºC, 0.8 ± 0.1 GPa, cor. 0.86. The core composition (Figure 5) has lower Mg content and probably reflects slightly lower temperature as garnet nucleates possibly at higher pressure given the higher Ca content. There is no evidence of garnet growth or re-equilibration by diffusion during cooling from peak metamorphic conditions.
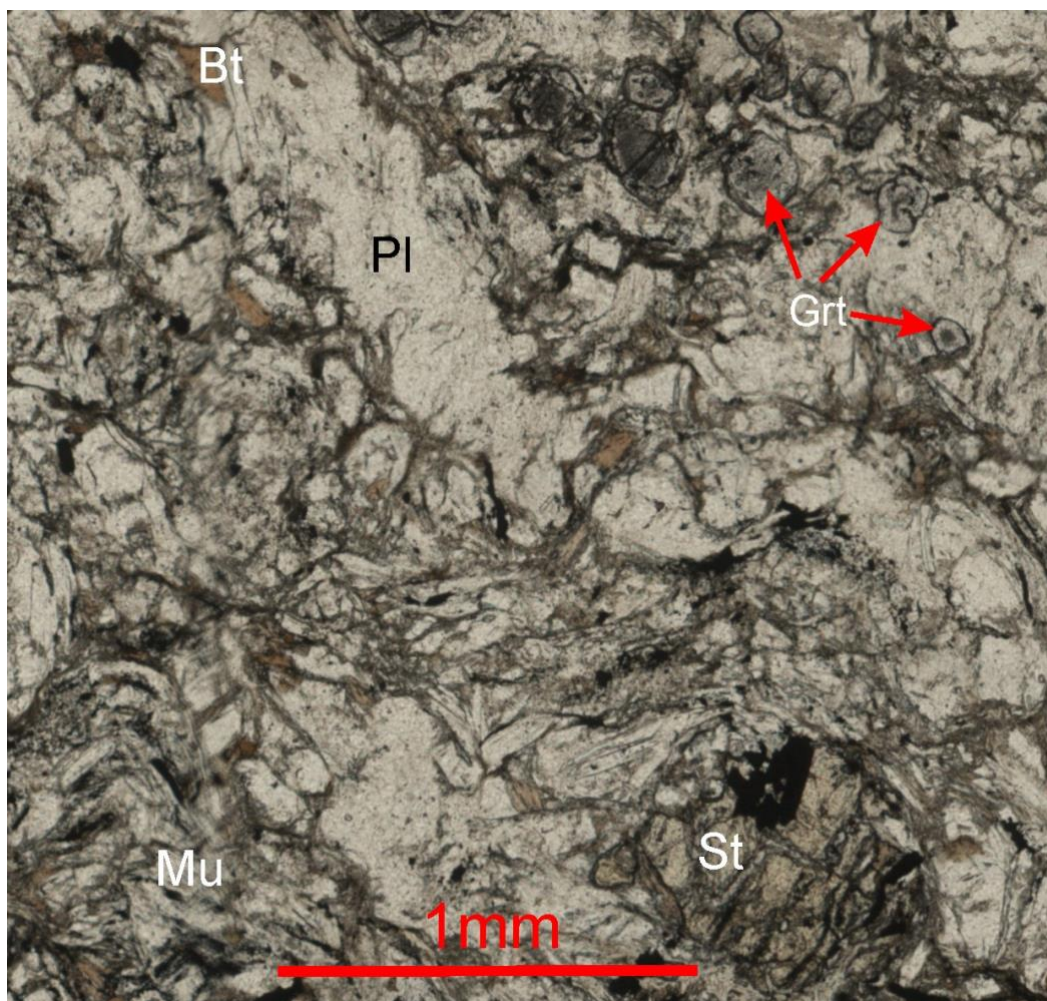
Figure 3. Transmitted light image of sample 63578. Staurolite grain at bottom middle. Small dark garnet grains with heavily included cores and clear rims. Larger plagioclase grains are moderately included. Field of view (horizontal) is 2.5 mm.

Sample 63727 is quartz–plagioclase–biotite–muscovite–margarite–staurolite–ilmenite gneiss from 300 m further west (Figure 1). The sample has large garnets up to 5 mm in a plagioclase rich matrix. Margarite occurs in a discrete band (Figure 6). The biotite is red brown. Quartz is in discrete bands, possibly early veins. The dominant foliation is intensely crenulated in more than one generation of folding. Garnet overgrows a strong Si defined by ilmenite that matches the orientation of the dominant foliation in the matrix. Some crenulations wrap around the garnet (Figure 6).

The garnet grain cores have relatively uniform Ca and Mg, but the rims are higher in Mg and lower in Ca (Figure 7). Using the rim compositions in Thermocalc v3.25 (Holland & Powell, 2013) the average P–T is given as 620 ± 24 ºC, 0.9 ± 0.1 GPa, corr. 0.86. The core composition (Figure 7) has lower Mg content and probably reflects slightly lower temperature as garnet nucleates. The high Ca spike on one side of the garnet is where the garnet is in contact with margarite and may reflect equilibrium with margarite rather than the plagioclase composition assumed in the P–T calculation.
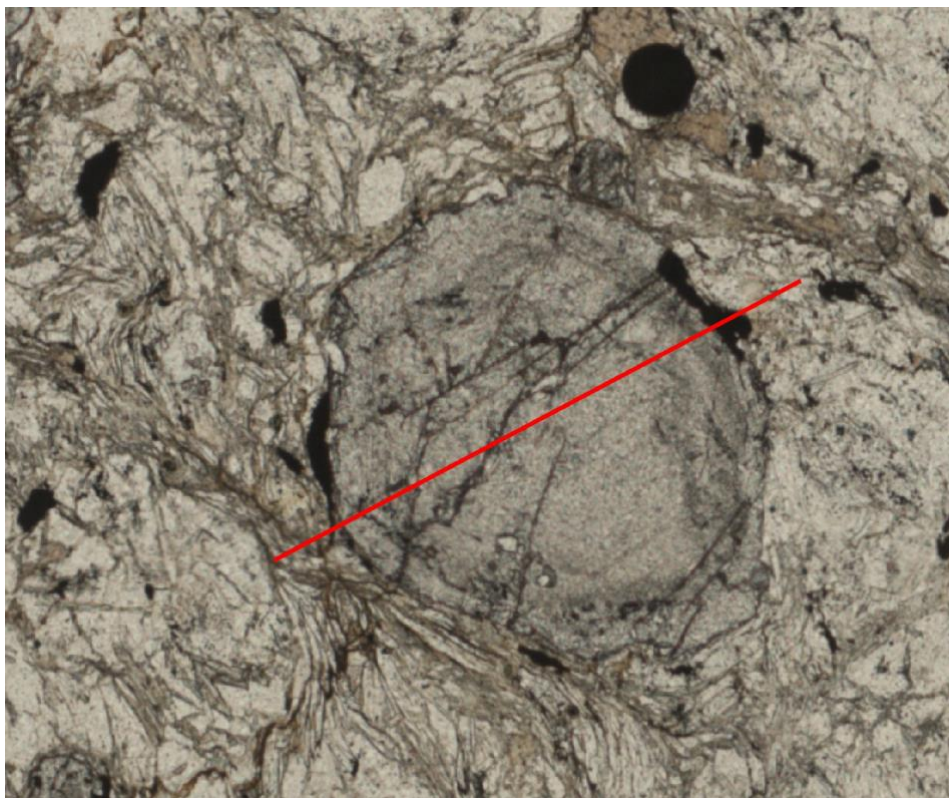
Figure 4. Sample 63578. Garnet grain used for zoning study shown in Figure 5. Garnet is 1 mm in diameter. Line of analyses shown in red.

Sample 63575 is from a further 700 m west (Figure 1). It is a quartz–plagioclase–biotite–muscovite–garnet gneiss with garnet to 5 mm diameter. Both quartz and plagioclase bands are common. The dominant foliation in the dark bands is complexly folded by multiple generation of crenulations but the Si in the garnet is straight (Figure 8) as with sample 63727. There is some retrograde chlorite, and this sample is more affected by clay alteration than the other gneisses discussed here.

There is very little zoning in the garnet (Figure 9). The garnet rim compositions were used with matrix grains to estimate the P–T conditions as 660 ± 30 ºC, 0.9 ± 0.1 Gpa, corr. 0.82 using Thermocalc 3.25 (Holland & Powell, 2013).
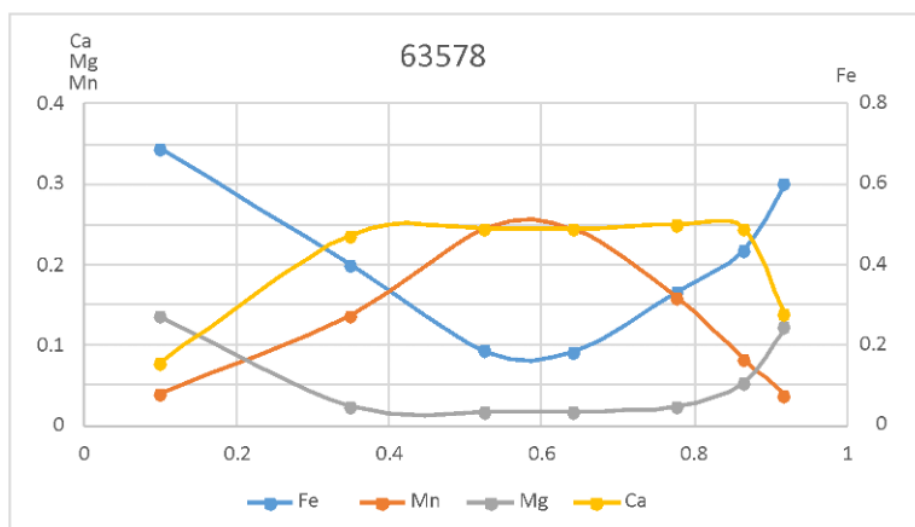
Figure 5. Compositional zoning in garnet from 63578. Note Fe cations scale shown on right of diagram. Horizontal axis is in mm.
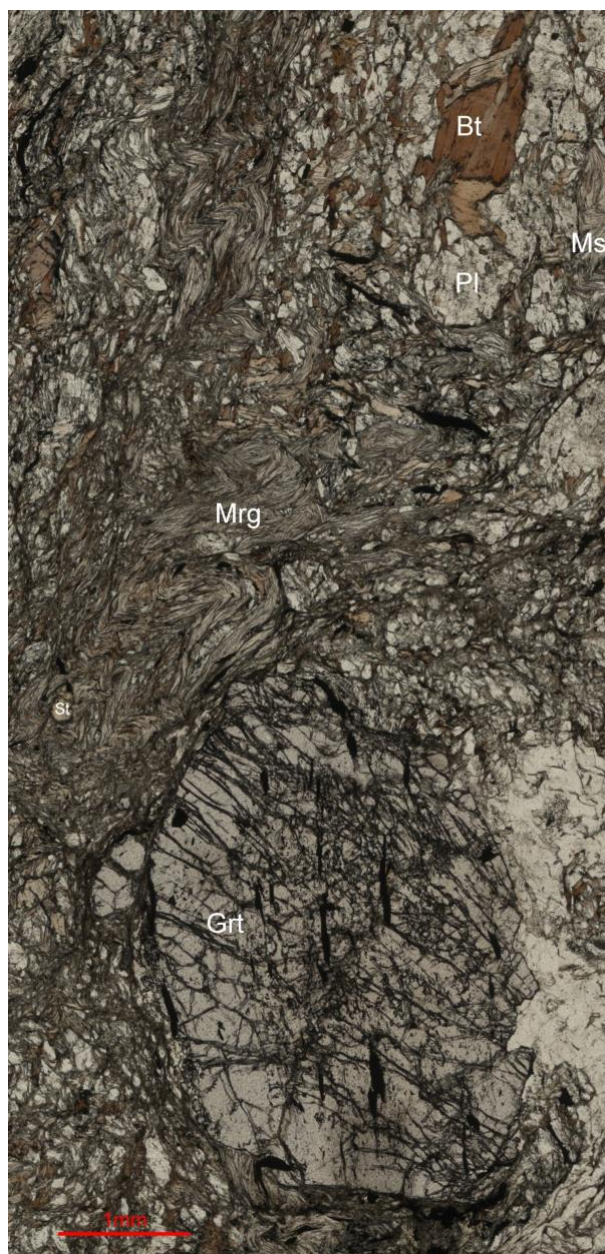
Figure 6. Sample 63727. Field of view 4.5 mm wide. With margarite (Mrg) and garnet.
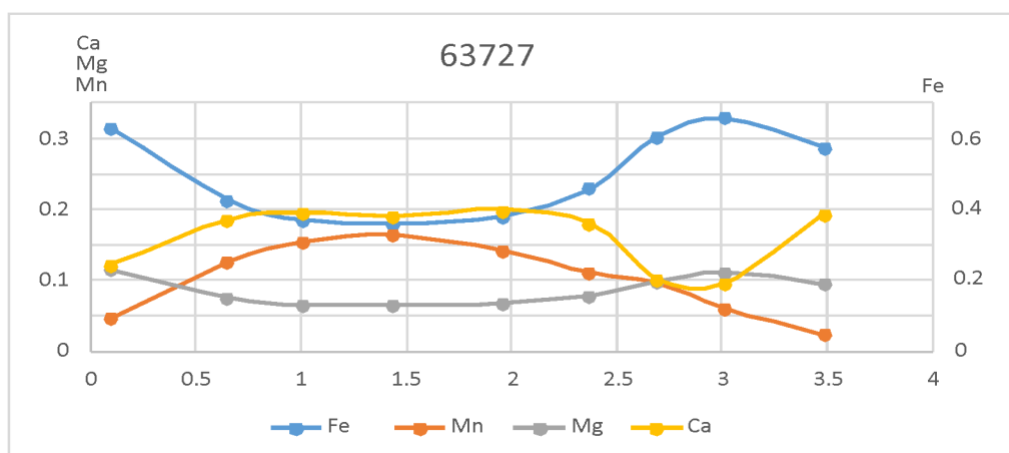

Figure 7. Compositional zoning in garnet from 63727. Note Fe cations scale shown on right of diagram. Horizontal axis is in mm.
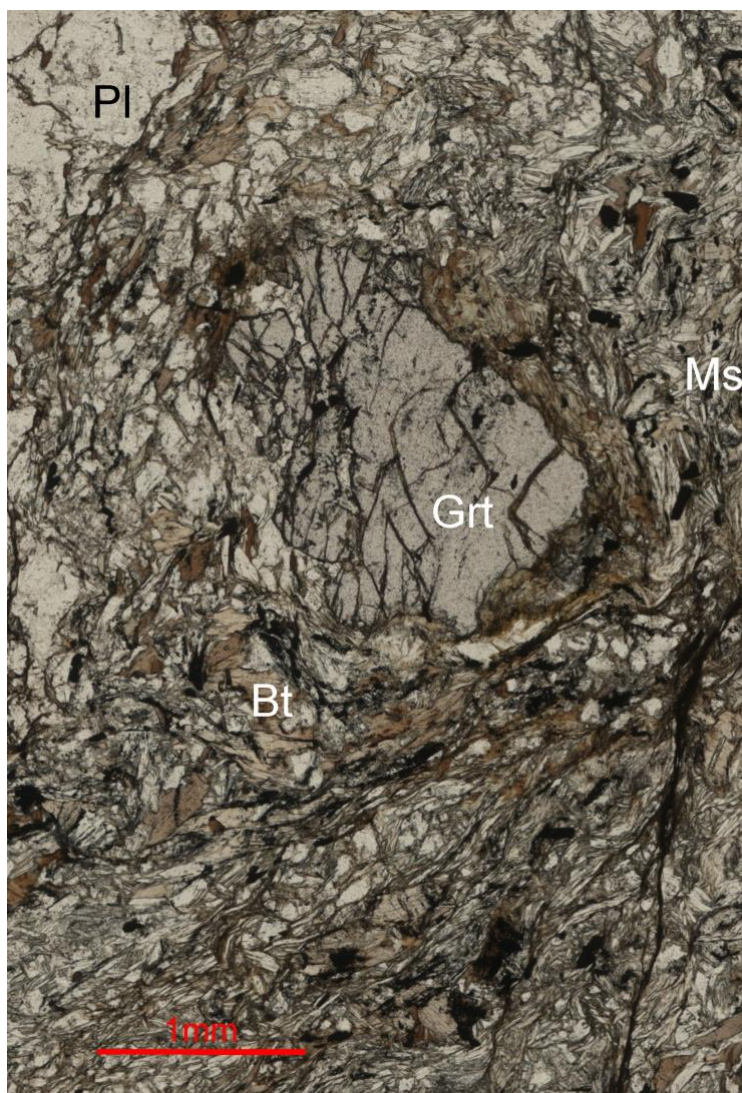
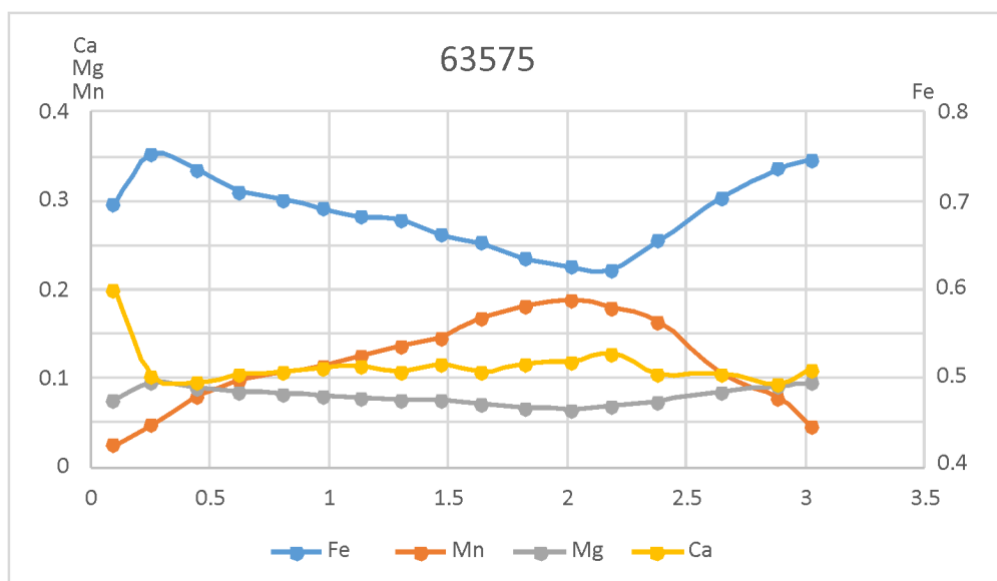*Figure 8. Sample 63575. Field of view 3.5 mm.*

Figure 9. Compositional zoning in garnet from 63575. Note Fe cations scale shown on right of diagram. Horizontal axis is in mm.

Sample 63579 is a quartz–plagioclase–biotite–muscovite–garnet schist. Retrograde chlorite is common. The fine grain size may reflect an early high strain history and there are rare grains of possibly porphyroclastic plagioclase. However, the texture lacks critical evidence for a mylonite origin possibly due to annealing. The largest garnet seen is 2 mm in diameter and has preserved a straight internal foliation (Si) of ilmenite, that is now at right angles to the dominant foliation (Figure 10). Using the rim garnet composition with matrix minerals a P–T of 650 ± 50 ºC, 1.2 ± 0.2 Gpa, corr. 0.93 was calculated using Thermocalc v3.25 (Holland & Powell, 2013).
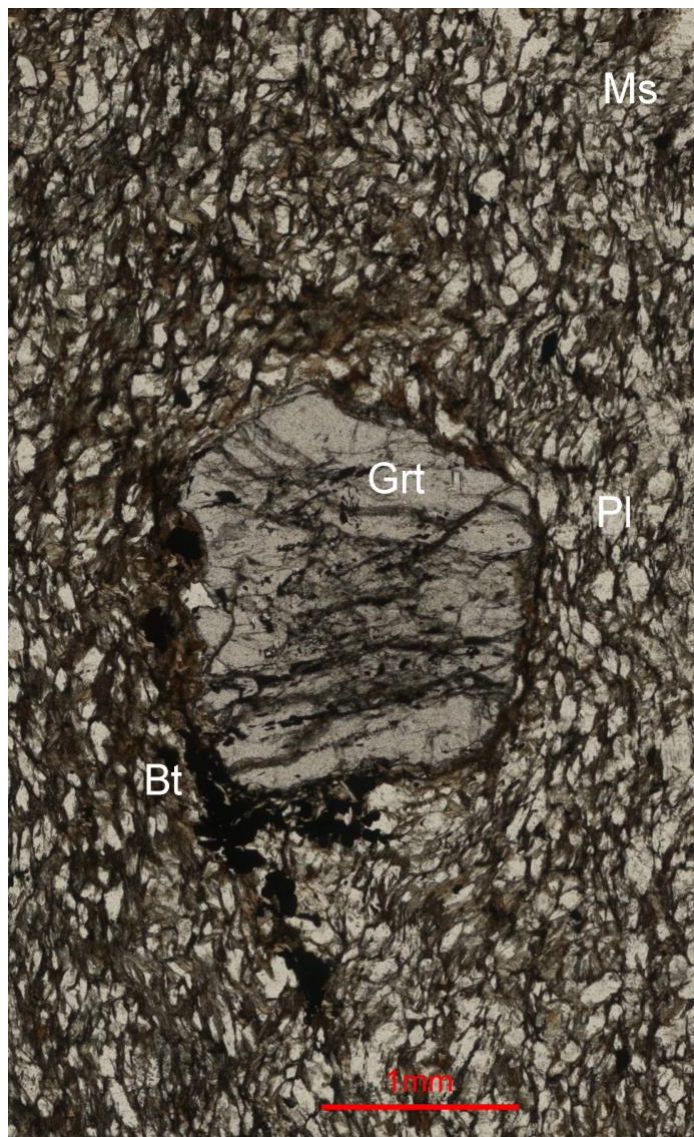

Figure 10. Sample 63579 showing large garnet with possible asymmetric foliation and internal foliation (Si) defined by ilmenite, at 90º to the external foliation (Se). The field of view is 3.5 mm wide.

63738

Sample 63738 comes from the far western margin of the Miomaffo massif. It has the same quartz–muscovite–biotite–staurolite–garnet mineralogy as other gneiss samples in the western sector. However, the early foliation preserved with the staurolite porphyroblasts and relict clasts (Figure 11) is much finer grained and appears to define isoclinal fold. The early foliations are apparently defined by graphite. The garnets grains are up to 3 mm diameter.

Figure 11. Photomicrograph of the sample 63738. Note the intense foliation preserved with the relict clasts and staurolite porphyroblasts. Field of view is 2.4 mm wide.
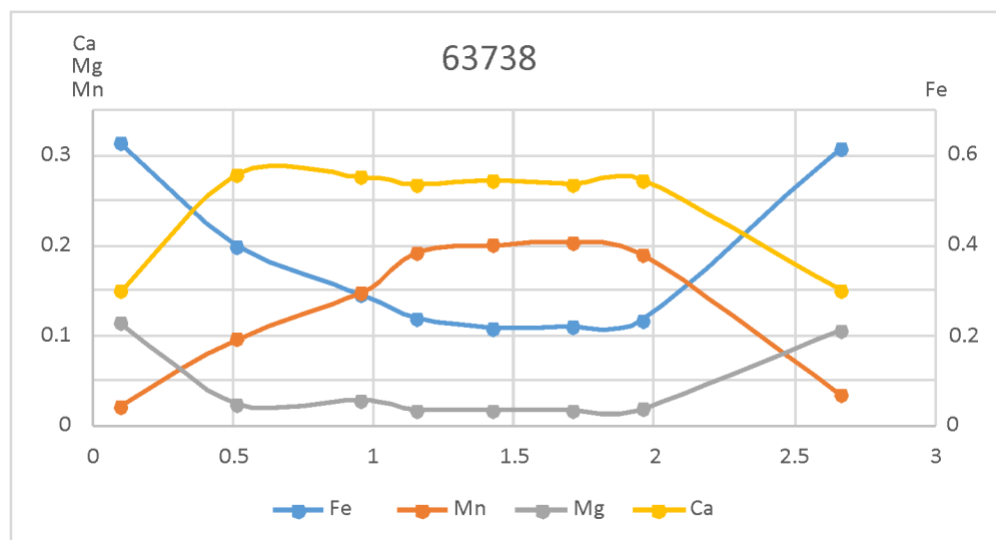
Figure 12. Compositional zoning in garnet from 63738. Note Fe cations scale shown on right of diagram. Horizontal axis is in mm.

The garnets show a constant composition across the core with a narrow rim that reflects higher Mg content and lower Ca. The rim composition gives a higher temperature result to other samples at similar pressures, 720 ± 30 ºC, 0.9 ± 0.1 Gpa, corr. 0.82 using Thermocalc v3.25 (Holland & Powell, 2013). The core compositions of garnet in this samples are consistent with a lower temperature and higher pressure.

Sample 63703 comes from the southern tip of the western sector. It is a quartz–biotite–muscovite–chlorite schist with trace garnet and ilmenite. It is lower in quartz than most of the other samples (Table 1) and has a small amount of K feldspar. The dominant foliation is strongly crenulated (Figure 13). The garnet is fractured and controls the position of one of the crenulation events. It is probably synchronous with the dominant foliation. The average P–T was calculated using the rim garnet composition as 600 ± 40 ºC, 1.0 ± 0.1 Gpa, corr. 0.93 using Thermocalc (Holland & Powell, 2013). The garnet is high Mn throughout and the zoning is very small. The average P–T conditions calculated from the rims of grains reflect conditions close to maximum metamorphic grade. The variation is small, and the average P–T condition is 650 ºC, 0.9 GPa.
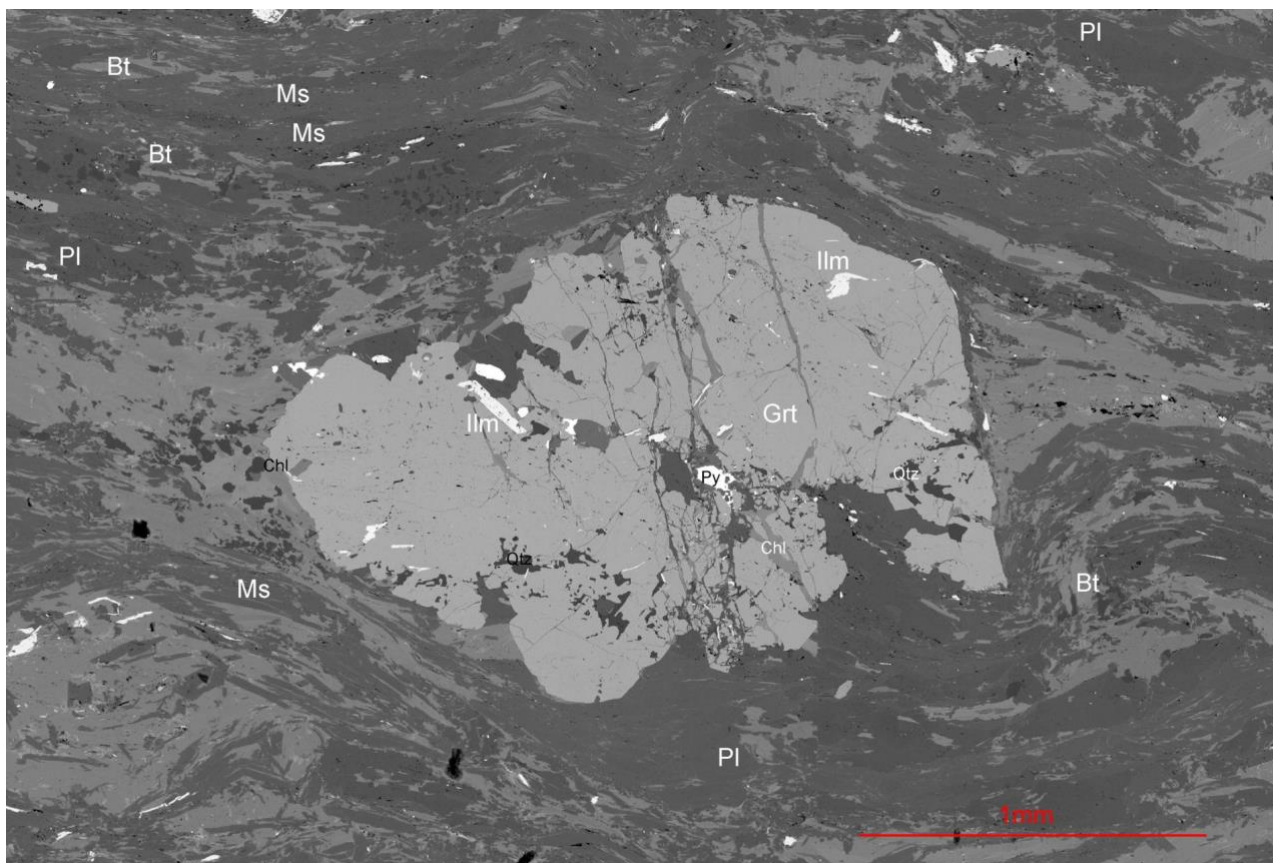
Figure 13. BSE image of sample 63703. The garnet grain is 2 mm long.
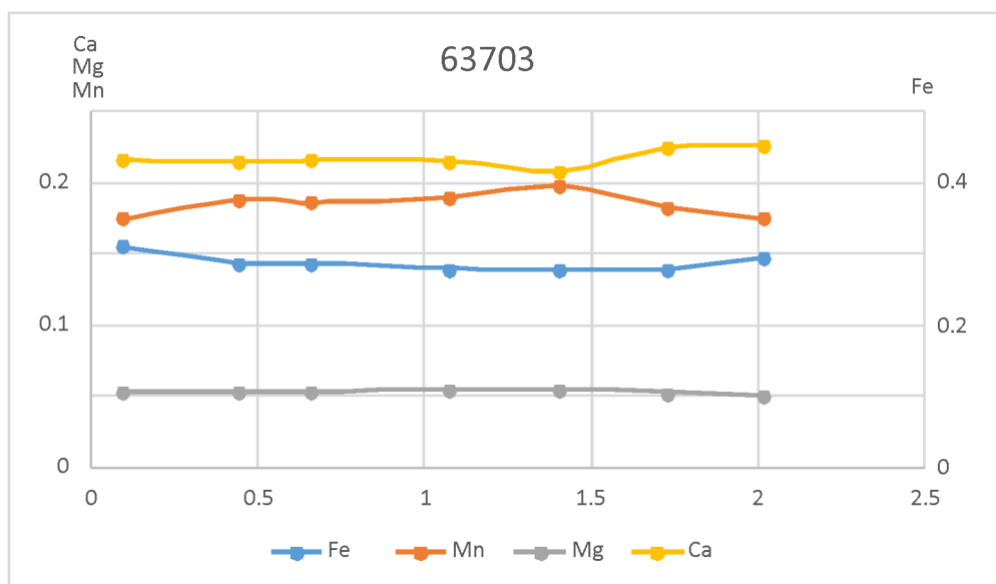

Figure 14. Compositional zoning in garnet from 63703. Note Fe cations scale shown on right of diagram. Horizontal axis is in mm.

All the P–T results are within error of each other (Figure 15). However, the evidence suggests the peak metamorphic T of the sample from the south is 50 ºC cooler than the other samples and this fits with the limited garnet, stabilised by high Mn, and the lack of staurolite in this sample. Sample 63738 apparently has higher temperature metamorphism than other samples. This sample comes from the far west, in an area with very limited outcrop. The field interpretation suggested it was across a major fault from the other northern samples. The data can best be explained if there is a consistent temperature across the north of the western sector until the metamorphic grade jumps at this fault contact. The variation in metamorphic grade does not appear to be the smooth gradient reported by Sopaheluwakan *et al.* (1989). One sample appears to be high

P than the others (63579). This sample is only 500 m west of 63575 so a large change in pressure of metamorphism is not likely. As the P–T estimates overlap at the 95% confidence level, we group all these samples together.

The metamorphism of the western sector is at slightly higher P and T than the conditions reported for the Mutis massif, 5 km to the west (Sopaheluwakan *et al.*, 1989). However, the inferred geothermal gradient is very similar at about 20 ºC/km. The medium P/T conditions reported from the Lacluta and Bebe Suza Massifs (Standley & Harris, 2009), 100 km to the east, reflect a higher geothermal gradient. The extremely high temperature conditions at low P reported from the Boi massif, 100 km to the west (Brown & Earle, 1983), reflect an additional localised heating event that has not been identified at Miomaffo or other blocks of Mutis Complex.
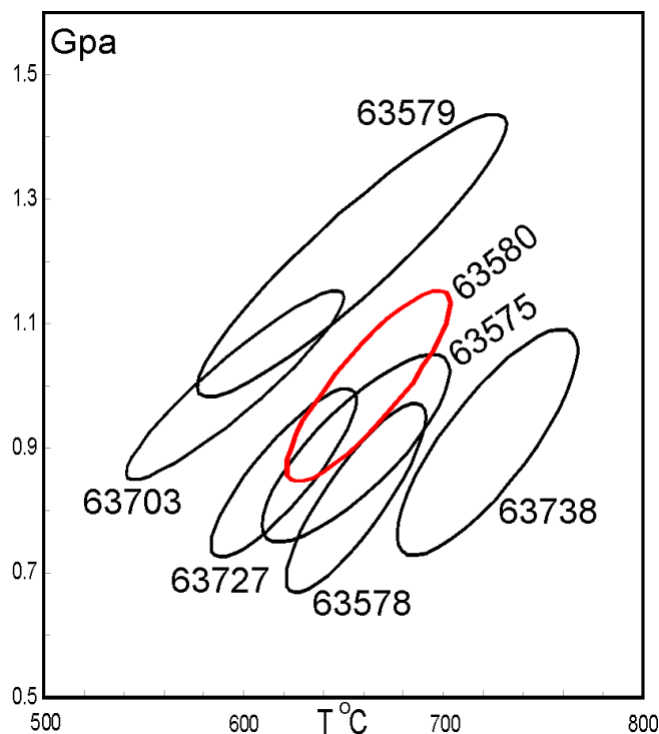

Figure 15. Average P–T for amphibolite facies samples in the Mutis Complex. The sample in red (63580) is from a block in the eastern sector. All other samples are from the western sector. P–T conditions calculated using rim garnet composition and Thermocalc v3.25.

References

Holland, T. J. B., & Blundy, J. (1994). Non-ideal interactions in calcic amphiboles and their bearing on amphibole–plagioclase thermometry. *Contributions to Mineralogy and Petrology*, 116, 433–447. https://doi.org/10.1007/BF00310910

Holland, T. J. B., & Powell, R. (2011). An improved and extended internally consistent thermodynamic dataset for phases of petrological interest, involving a new equation of state for solids. *Journal of Metamorphic Geology*, *29*, 333–383. https://doi.org/10.1111/j.1525-1314.2010.00923.x

Kohn, M. J., & Spear, F. S. (1993). Phase equilibria of margarite-bearing schists and chloritoid + hornblende rocks from Western New Hampshire, USA. *Journal of Petrology*, 34, 631–651. https://doi.org/10.1093/petrology/34.4.631

Powell, R., & Holland, T. J. B. (2008). On thermobarometry. *Journal of Metamorphic Geology, 26*, 155–179. https://doi.org/10.1111/j.1525-1314.2007.00756.x

Sopaheluwakan, J., Helmers, H., Tjokrosapoetro, S., & Surya Nila, E. (1989). Medium pressure metamorphism with inverted thermal gradient associated with ophiolite nappe emplacement in Timor. *Netherlands Journal of Sea Research*, *24,* 333–343. https://doi.org/10.1016/0077-7579(89)90159-2

Standley, C., & Harris, R. A. (2009) Banda forearc basement accreted to the NW Australian continental margin: a geochemical, age and structural analysis of the Lolotoi metamorphic complex of East Timor. *Tectonophysics*, 479, 66–94. https://doi.org/10.1016/j.tecto.2009.01.034

Whitney, D. L., & Evans, B. W. (2010). Abbreviations for names of rock-forming minerals. *American Mineralogist*, 95, 185–187. https://doi.org/10.2138/am.2010.3371

Supplemental data 6. U/Pb Apatite age for a garnet gneiss of the Mutis Complex, Miomaffo

The apatite grains in some garnet gneiss samples from the western sector are unusually large (up to 1 cm) and are in textural equilibrium with the metamorphic assemblage. Two of these samples were analysed by LA-ICP-MS using methods as described in Supplemental data 4. One of these samples (Figure 1) had sufficient U in the apatite to provide an age constraint on the metamorphic age.
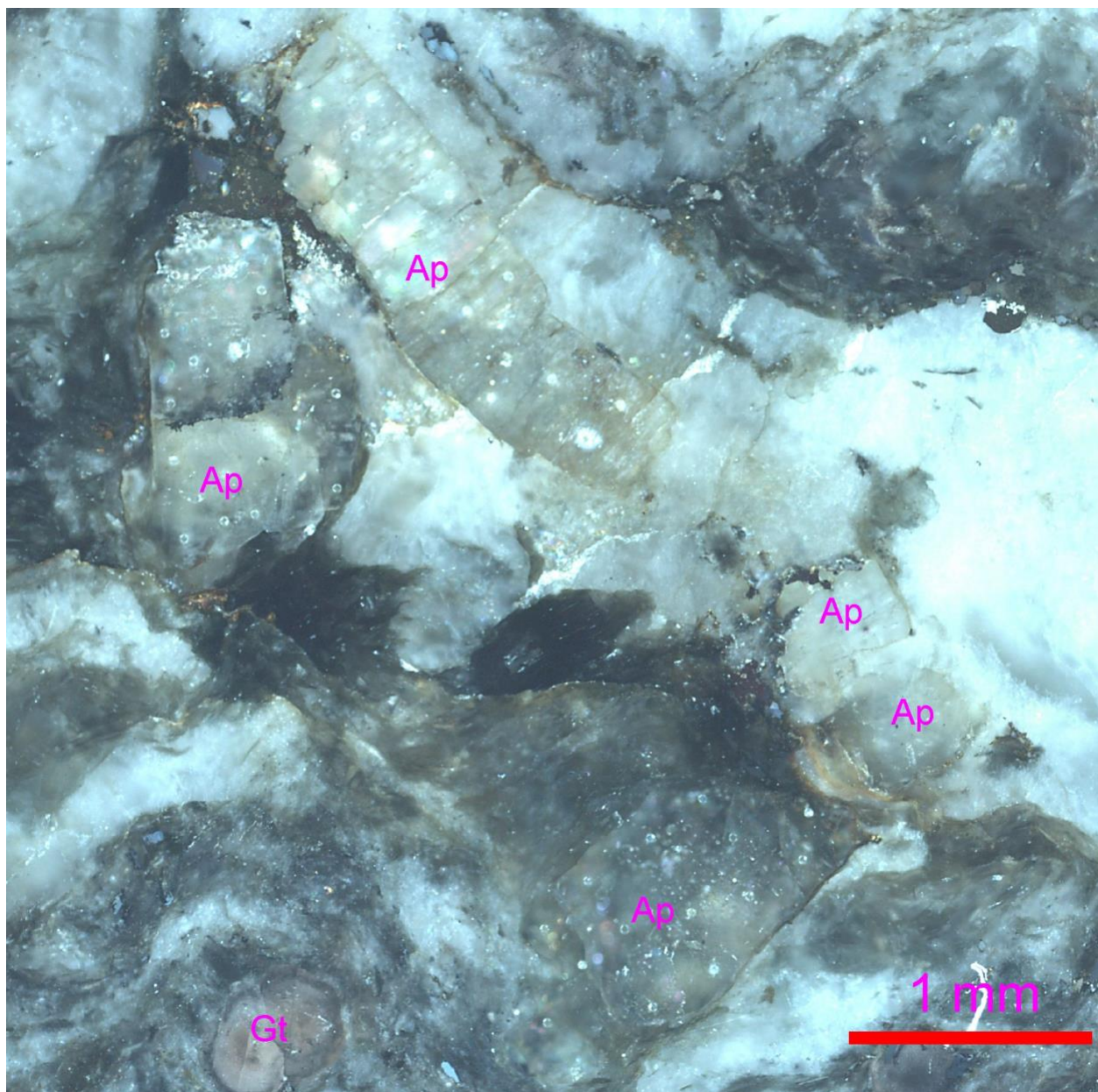

Figure 1. Reflected light cross-polarised image of apatite grains in garnet (Gt) bearing felsic gneiss (63725) showing apatite (Ap) grains. White circles in apatite are laser pits.

For sample 63725 (see Supplemental data 4, Figure 1. for location) several of the large grains were analysed by LA-ICP-MS (Table 1). The apatite has about 5 ppm U and the ratio of radiogenic to common Pb is very low. However, based on 45 spots a model age for the metamorphism of 31 ± 23 Ma was achieved (Figure 2). This result supports the textural interpretation that these apatite porphyroblasts grew during the metamorphic event. They are within error of $^{40}Ar/^{39}Ar$ hornblende ages from nearby rocks (Supplemental data 3).
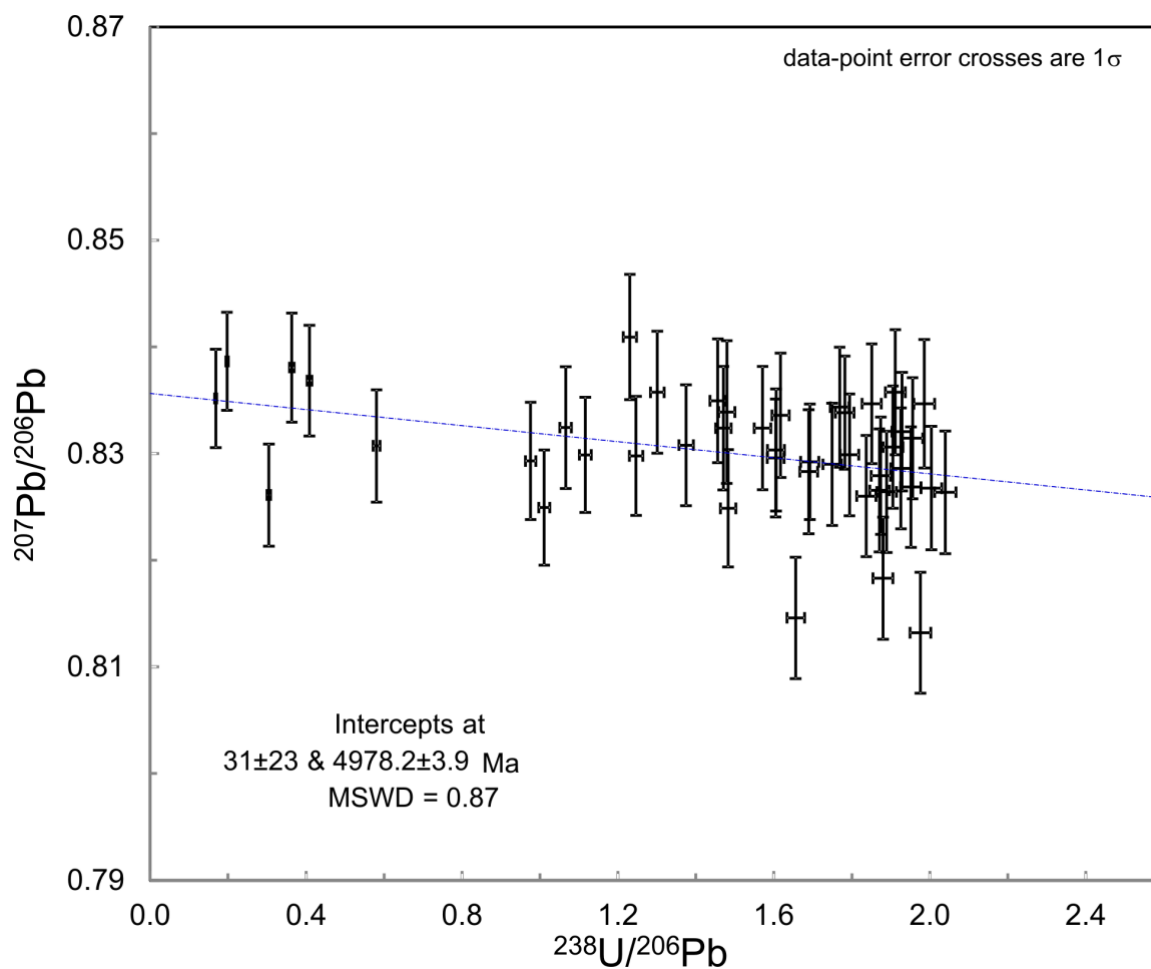
Figure 2. Inverse concordia diagram for apatite analyses in sample 63725. One sigma error cross shown for each point. Diagram drawn using Isoplot (Ludwig, 2008).

Reference

Ludwig, K. R. (2008). User's manual for Isoplot 3.6, a geochronological toolkit for Microsoft Excel. Berkeley Geochronology Center.